Computers and Geotechnics 193 (2026) 107918

Contents lists available at ScienceDirect

Computers and Geotechnics

journal homepage: www.elsevier.com/locate/compgeo

Research paper

A graph-based algorithm for the Continuous-Projection Embedded Discrete Fracture Model (CpEDFM-U) to simulate two-phase flows in naturally fractured porous media using the MPFA-D method on general unstructured meshes

Gabriel Martins Cavalcanti Feitosa [a,*], Emanoel Rodrigues dos Santos [b], Pedro Victor Paixão Albuquerque [b], Artur Castiel Reis de Souza [c], Darlan Karlo Elisiário de Carvalho [a], Paulo Roberto Maciel Lyra [b]

[a] Universidade Federal de Pernambuco, Departamento de Engenharia Mecânica, Av. da Arquitetura s/n, Recife, 50740-550, PE, Brazil
[b] Universidade Federal de Pernambuco, Departamento de Engenharia Civil, Rua Acadêmico Hélio Ramos s/n, Recife, 50740-530, PE, Brazil
[c] TNO, Netherlands

ARTICLE INFO

Keywords:
Numerical simulation
Oil and water displacements in 2D
Naturally fractured porous media
CpEDFM-U
MPFA-D
Unstructured meshes

ABSTRACT

Modeling fluid flow in naturally fractured porous media is crucial for applications such as hydrocarbon production and CO2 sequestration. However, accurately simulating these flows remains challenging due to fractures with complex permeability distributions. The Embedded Discrete Fracture Model (EDFM) has been widely used but has limitations in representing fractures acting as barriers, especially in multiphase flows. To overcome these challenges, the Projection-based Embedded Discrete Fracture Model (pEDFM) was developed, offering better handling of fractures with lower permeability than the matrix. However, it can still exhibit discontinuities in fracture projections. To address these limitations, we propose the Continuous-Projection Embedded Discrete Fracture Model (CpEDFM-U), a graph-based algorithm that guarantees continuous fracture projections in both structured and unstructured 2D meshes. The CpEDFM-U uses Dijkstra's algorithm to find the shortest path between fracture tips and applies the MPFA-D method for matrix flow and TPFA for fractures. In numerical simulations analyzed, CpEDFM-U outperforms EDFM and pEDFM, demonstrating lower errors and robust performance across different fracture types and mesh resolutions.

1. Introduction

Accurate and efficient modeling of fluid flow in fractured porous media is crucial for a variety of geotechnical and subsurface engineering applications, including hydrocarbon production, CO_2 sequestration, and geothermal energy extraction. Fractures often dominate the flow behavior, even though they occupy a relatively small volume compared to the surrounding rock matrix (Berkowitz, 2002). Capturing this influence without excessively increasing the computational burden remains a significant challenge in numerical modeling.

Explicit fracture modeling approaches fall broadly into two categories: conforming and non-conforming methods. Mesh-conforming methods, such as discrete fracture models (DFM), explicitly represent fractures within the computational mesh by aligning grid cells with fracture geometries. Fractures are modeled as lower-dimensional entities (e.g., 2D surfaces in 3D domains), and the mesh is refined to ensure that fracture surfaces conform exactly to element faces. This allows accurate resolution of pressure and flux discontinuities at the fracture–matrix interface using different discretization methods (Karimi-Fard and Firoozabadi, 2003; Karimi-Fard et al., 2004; Burbulla and Rohde, 2020; Cavalcante et al., 2020; Berre et al., 2021; Teixeira et al., 2022; Rao et al., 2024a; Wang et al., 2022). However, the requirement of mesh conformity introduces significant computational challenges, especially when modeling complex or large-scale fracture networks in 3D. The meshing process becomes increasingly costly and fragile in the presence of small fractures, acute intersections, or densely connected networks (Karimi-Fard et al., 2004). In 3D domains, generating high-quality conforming meshes often demands sophisticated algorithms and may still produce highly skewed or distorted elements that degrade numerical performance. Recent advances, such as those presented in de Hoop et al. (2022), have improved the robustness of conforming mesh

* Corresponding author.
E-mail address: gabriel.gmcf@ufpe.br (G.M.C. Feitosa).

https://doi.org/10.1016/j.compgeo.2026.107918
Received 18 August 2025; Received in revised form 24 December 2025; Accepted 8 January 2026
Available online 27 January 2026

workflows, yet these methods remain limited by their scalability and preprocessing overhead. Consequently, the limitations of conforming DFMs have driven the development of non-conforming or embedded approaches, which decouple discrete fracture representation from the matrix mesh generation and allow for more flexible and efficient modeling of fractured systems (Li and Lee, 2008; Ţene et al., 2017; Jiang and Younis, 2017).

As an alternative, Embedded Discrete Fracture Models (EDFM) formulations represent fractures as discrete lower-dimensional entities embedded into a matrix grid, eliminating the need for mesh conformity to fracture geometry (Shakiba, 2014). In EDFM, matrix and fractures can be meshed independently, while they exchange flux with surrounding matrix cells through non-neighboring connections (NNCs), enabling efficient simulation of complex or dense fracture networks while maintaining structured grids in the matrix. Due to these characteristics, EDFM has seen its widespread use (Li and Lee, 2008; Hajibeygi et al., 2011; Moinfar et al., 2014; Yu et al., 2018; Dachanuwattana et al., 2018; Fumagalli et al., 2019; Wang et al., 2023; Xu et al., 2023; Zeng et al., 2019; Mejia et al., 2021). While EDFM offers flexibility and computational efficiency, it has limitations. For example, EDFM is not capable of capturing barrier effects (Ţene et al., 2017; Jiang and Younis, 2017) and it computes fluxes incorrectly in multiphase flow (Jiang and Younis, 2017).

To overcome specific limitations of the standard EDFM in modeling multiphase flow through fractured porous media, the projection-based Embedded Discrete Fracture Model (pEDFM) was developed (Ţene et al., 2017; Jiang and Younis, 2017). The pEDFM works by projecting fractures onto cell faces, weakening the connections between cells that share a face that received the projection, and creating NNCs between the fracture cells and both cells sharing the projected face. At the cost of a marginal increasing in computational cost, the pEDFM is capable of fixing the aforementioned limitations of the EDFM. The pEDFM was also developed extensively (Ren et al., 2018; Olorode et al., 2020; Rao et al., 2020; HosseiniMehr et al., 2022; Rao, 2023; Rao et al., 2024b, 2025), using structured meshes and was extended to for unstructured tetrahedral mesh meshes by Cavalcante et al. (2024).

However, the algorithm used to compute which faces will receive projections is crucial for a consistent pEDFM. Ţene et al. (2017) suggested an algorithm which was improved by Jiang and Younis (2017). The algorithm consists of highlighting a pair of matrix cell faces which are the closest to the fracture, ensuring they are on the same side of the fracture. This was done to guarantee a set of projection faces that would yield a physical projection configuration. Later, Rao and Liu (2022) extended the idea of physical projection configuration, proposing the Equivalence theorem. The theorem states that the projection configuration of a fracture being physical is equivalent to it being topologically homeomorphic to the fracture. Therefore, from a geometric point of view, the topological properties of the projection configuration are the same as those of the fracture. Rao and Liu (2022) and Rashid and Olorode (2024) showed that the standard pEDFM algorithm was insufficient to guarantee a physical configuration space. In some cases the projection configuration have holes, which makes the projection configuration not homeomorphic to the fracture, and leakage can occur in low permeability fractures. Rashid and Olorode (2024) proposed the first algorithm that guarantees a continuous projection, the CpEDFM, thereby ensuring physical consistency for structured meshes.

Similar to Rao et al. (2024b), in the present work we use a locally conservative discretization that is robust and consistent for unstructured meshes. However, the authors used the general pEDFM framework, proposed by Rao (2023), which, for high-conductivity fractures uses a standard pEDFM, with the micro-translation method to obtain the projection path, while using a non-projective, average transmissibility method for barriers. The general pEDFM together with the hybrid TPFA-MFD method for matrix flux computation make their numerical framework very robust and general. Meanwhile, in the present work, we use the standard pEDFM approach but we develop a new strategy based on the Dijkstra's algorithm to obtain a continuous projection path, that works on both cartesian and general unstructured 2D meshes, together with a non-orthodox Multipoint Flux Approximation Method based on a Diamond Stencil (MPFA-D).

In this work, we propose a robust and general algorithm, the so-called Continuous Projection Embedded Fracture Model for Unstructured Meshes (CpEDFM-U), to ensure continuous and consistent projection behavior within the pEDFM framework. The algorithm consists into mapping cells nodes to graphs, computing the shortest path between fracture ends through the graph, then mapping the path chosen back to the matrix faces, which would consist on being the projection configuration. Since the shortest path between two nodes in a graph is continuous, the projection configuration will be continuous by extension (Dijkstra, 2022). One of the advantages of our methodology is that the algorithm works on both structured and general unstructured 2D meshes. Through a series of numerical experiments, we demonstrate that the proposed algorithm improves on the standart pEDFM method, ensuring a continuous projection, both on structured and unstructured meshes.

The main contributions of this paper are a novel algorithm for determining fracture projections, using graph mapping and Dijkstra's algorithm, that ensures continuous fracture projections in both cartesian and unstructured meshes, together with the robust Multi-point Flux Approximation Method with Diamond Stencil, MPFA-D, capable of handling both cartesian and general 2D unstructured meshes, under the standard pEDFM framework.

The remainder of the paper is divided into four sections: Section 2 we show the mathematical model employed, Section 3 we describe our new numerical formulation used, Section 4 we present the numerical results obtained using the proposed methodology and in Section 5 draws some concluding remarks.

2. Mathematical model

In this section, we briefly describe the mathematical model for isothermal, immiscible and incompressible two-phase flow in naturally fractured reservoirs. We also consider the rock matrix to be incompressible. Considering a 2D matrix domain Ω_m containing fractures Ω_{f_k}, it is possible to define the mass conservation equation for each fluid phase in which the terms related to the rock matrix are represented by the index m, and those related to the kth fracture within the domain are represented by f_k. For each phase $\alpha = o$ (oil) and $\alpha = w$ (water), we have the following equation (Cavalcante et al., 2024):

$$\phi \frac{\partial}{\partial t}(S_\alpha)_m + \nabla \cdot (\vec{v}_\alpha)_m = (q_\alpha)_m + \sum_{k=1}^{n_{frac}} (\varphi_\alpha)_{m,f_k} \tag{1}$$

where the variables ϕ, S_α, n_{frac} and $(q_\alpha)_m$ represent the medium porosity, the saturation of phase α, the number of fractures within the domain Ω_m and source/sink terms, respectively. $(\varphi_\alpha)_{m,f_k}$ represents the phase transfer between Ω_m and Ω_{f_k}. The velocity $\vec{v}_\alpha$ is given by Darcy's law, which without considering gravity and capillarity effects can be written as $\vec{v}_\alpha = -\lambda_\alpha K \nabla p$, where the phase mobility is given by $\lambda_\alpha = k_{r\alpha}/\mu_\alpha$ with $k_{r\alpha}$ and μ_α being the relative phase permeability and viscosity, respectively. K is the rock absolute permeability tensor and p is the fluid pressure. Similarly to Eq. (1), the mass conservation equation for the *k-th* fractures in the domain Ω_{f_k}, for a phase α can be written as:

$$\omega\phi \frac{\partial}{\partial t}(S_\alpha)_{f_k} + \omega \nabla \cdot (\vec{v}_\alpha)_{f_k} = (q_\alpha)_{f_k} + (\varphi_\alpha)_{f_k,m} + \sum_{j=1}^{n_{frac}} (\varphi_\alpha)_{f_k,fl;\ ,\ l\neq k} \tag{2}$$

where ω is the fracture aperture, $(q_\alpha)_{f_k}$, $(\varphi_\alpha)_{f_k,m}$, $(\varphi_\alpha)_{f_k,f_j}$ represents source or sink terms, the phase transfer term between Ω_{f_k} and Ω_m and between Ω_{f_k} and Ω_{fl}, respectively. All of the mass transfer terms between matrix and fractures, and between intersecting fractures will be defined in Section 3.

It is worth highlighting that the matrix domain is 2D whereas the fracture domains are 1D. We consider also that the media is fully saturated, i.e.:

$$S_w + S_0 = 1 \tag{3}$$

Using the mass conversation law defined by (1) and (2) along with (3), and after some algebraic manipulations, we can write the mathematical model as:

$$\phi \frac{\partial}{\partial t}(S_w)_m + \nabla \cdot (f_w \vec{v})_m = (q_w)_m + \sum_{k=1}^{n_{frac}} (f_w \varphi)_{m,f_k} \tag{4}$$

$$\nabla \cdot (v)_m = (q)_m + \sum_{k=1}^{n_{frac}} (\varphi)_{m,f_k} \tag{5}$$

for the matrix and for the fracture, we can write:

$$\omega\phi \frac{\partial}{\partial t}(S_w)_{f_k} + \omega\nabla \cdot (f_w \vec{v})_{f_k} = (q_w)_{f_k} + (f_w\varphi)_{m,f_k} + \sum_{j=1}^{n_{frac}} (f_w\varphi)_{f_k,f_j} \tag{6}$$

$$\omega\nabla \cdot (v)_{f_k} = (q)_{f_k} + (\varphi)_{m,f_k} + \sum_{j=1}^{n_{frac}} (\varphi)_{f_k,f_j} \tag{7}$$

in which $q = q_w + q_o$ denotes the total source term and $\vec{v} = \vec{v}_w + \vec{v}_o$ denotes the total fluid velocity. Furthermore $f_w = \lambda_w/\lambda$ is the water fractional flow, and $\lambda = \lambda_w + \lambda_o$ is the total mobility (Chen et al., 2007).

2.1. Initial and boundary conditions

The problem given by Eqs. (4) to (7) is completely determined if an appropriate set of initial and boundary conditions is defined:

$$\begin{aligned} p(x,t) &= p_D, && \text{on} \quad \Gamma_m^D \times [0,t], \\ \vec{v}.\vec{n} &= \bar{g}_{p,N}, && \text{on} \quad \Gamma_m^N \times [0,t], \\ p(x,t) &= p_{well} && \text{on} \quad \Gamma_m^w \times [0,t], \\ S_w(x,0) &= S_{w0}, && \text{on} \quad \Omega_m. \end{aligned}$$

where Γ_m^D and Γ_m^N are the boundaries with Dirichlet and Neumann conditions, respectively. The Γ_m^w indicates the well (with $w = I$ or P for injector and producer, respectively). Furthermore, t is the time variable, p_D and $p_{w,1}$ are known scalar functions representing the pressure, while $\bar{g}_{p,N}$ are know scalar functions representing the flux. Additionally, $\vec{n}$ is the unit outward normal vector to the control surface, $\vec{v} = \vec{v}_w + \vec{v}_o$ is the total velocity of the fluid, $S_w(x,0)$ is the initial reservoir distribution of water saturation. Moreover, it is important to note that we consider every single fracture to be completely contained in Ω_m, thus they have zero flux boundary conditions

3. Numerical formulation

In this section, we present the numerical formulation used to simulate the two-phase flow problem described by Eqs. (4) to (7), along with the appropriate initial and boundary conditions, in fractured reservoirs using 2D general meshes. Starting from a known saturation distribution, the fluid mobilities within the domain are calculated. Both saturation and mobility fields serve as inputs to a segregated IMPES formulation, where pressure is solved implicitly. Once the pressure field is obtained, fluxes across the domain are computed using Darcy's law. These velocities are then used to solve the saturation equation explicitly at each time step. The updated saturation field is used to recalculate mobilities, which are then fed back into the pressure solver. This iterative process continues until the end of the simulation.

3.1. Finite volume formulation

The first step of our numerical modeling is to discretize the matrix domains Ω_m into N_m cells $\Omega_{\hat{m}_i}$, so the ith matrix cell is indexed as $\hat{m}_i$. Furthermore the kth fracture domain Ω_{f_k} is discretized into N_f^k fracture cells $\Omega_{\hat{f}_k^j}$ such that the j-ith fracture cell is indexed as $\hat{f}_k^i$. Starting from the Eqs. (4) to (7) in integral form, then applying the divergence and mean value theorems, we obtain the following discrete expressions:

$$(Sw)_{\hat{m}_i}^{n+1} = (Sw)_{\hat{m}_i}^n - \mathcal{A}_{\hat{m}_i} \left(\sum_{j=1}^{N_m} (\mathcal{F}_{adv})_{\hat{m}_i,\hat{m}_j}^n + (Q_w)_{\hat{m}_i}^n + \sum_{k=1}^{n_{frac}} (\mathcal{F}_{adv})_{\hat{m}_i,f_k}^n \right) \tag{8}$$

$$\mathcal{A}_{\hat{m}_i} = \frac{\Delta t}{\phi_{\hat{m}_i} |\Omega_{\hat{m}_i}|} \tag{9}$$

$$\sum_{j=1}^{n_m} (\mathcal{F}_{diff})_{\hat{m}_i,\hat{m}_j} = (Q)_{\hat{m}_i}^n + \sum_{k=1}^{n_{frac}} (\mathcal{F}_{diff})_{\hat{m}_i,f_k} \tag{10}$$

for the matrix and for the fracture as:

$$(Sw)_{\hat{f}_k^i}^{n+1} = (Sw)_{\hat{f}_k^i}^n - \mathcal{A}_{\hat{f}_k^i} \left(\omega_{\hat{f}_k^i} \sum_{j=1}^{N_f} (\mathcal{F}_{adv})_{\hat{f}_k^i,\hat{f}_k^j}^n + (Q_w)_{\hat{f}_k^i}^n + (\mathcal{F}_{adv})_{\hat{f}_k^i,\hat{m}_i}^n + \sum_{l=1}^{n_{frac}} (\mathcal{F}_{adv})_{\hat{f}_k^i,\hat{f}_l^i}^n \right) \tag{11}$$

$$\mathcal{A}_{\hat{f}_k^i} = \frac{\Delta t}{\phi_{\hat{f}_k^i}, \omega_{\hat{f}_k^i} |\Omega_{\hat{f}_k^i}|} \tag{12}$$

$$\sum_{j=1}^{N_f} (\mathcal{F}_{diff})_{\hat{f}_k^i,\hat{f}_k^j} = (Q)_{\hat{f}_k^i}^n + (\mathcal{F}_{diff})_{\hat{f}_k^i,\hat{m}_i} + \sum_{l=1}^{n_{frac}} (\mathcal{F}_{diff})_{\hat{f}_k^i,\hat{f}_l^i} \tag{13}$$

where $(Sw)_{\hat{m}_i}$ and $(Sw)_{\hat{f}_k^i}$ are the average saturation at cells $\hat{m}_i$ and $\hat{f}_k^i$. $\Delta t = t^{n+1} - t^n$ is the time step. $\phi_{\hat{m}_i}$ and $\phi_{\hat{f}_k^i}$ are the average porosity for cells $\hat{m}_i$ and $\hat{f}_k^i$. $|\Omega_{\hat{m}_i}|$ is cell $\hat{m}_i$ area, while $|\Omega_{\hat{f}_k^i}|$ is cell $\hat{f}_k^i$ length. $\mathcal{F}_{adv}$ and $\mathcal{F}_{diff}$ are the diffusive and advective fluxes, which will be defined soon. Q_w and Q are the water and total source term. It is important to highlight that, in order to ensure mass conservation, the following expressions hold:

$$(\mathcal{F}_{adv})_{\hat{m}_i,f_k} = -(\mathcal{F}_{adv})_{f_k\hat{m}_i}, \; (\mathcal{F}_{diff})_{\hat{m}_i,f_k} = -(\mathcal{F}_{diff})_{f_k\hat{m}_i} \tag{14}$$

$$(\mathcal{F}_{diff})_{\hat{f}_k^i,\hat{f}_l^i} = -(\mathcal{F}_{diff})_{\hat{f}_l^i,\hat{f}_k^i}, \; (\mathcal{F}_{diff})_{\hat{f}_k^i,\hat{f}_l^i} = -(\mathcal{F}_{diff})_{\hat{f}_l^i,\hat{f}_k^i} \tag{15}$$

3.2. Neighbor diffusive fluxes

The matrix diffusive flux $(\mathcal{F}_{diff})_{\hat{m}_i,\hat{m}_j}$ between matrix cells $\hat{m}_i$ and $\hat{m}_j$ is the flux crossing the edge IJ as shown in Fig. 1. The edge IJ is composed by the nodes I and J, $h_{\hat{m}_i}$ and $h_{\hat{m}_j}$ are the heights relative to the centroids of $\hat{m}_i$ and $\hat{m}_j$, respectively. $\vec{n}_{IJ}$ is the unit normal vector to the edge IJ.

The matrix diffusive $(\mathcal{F}_{diff})_{\hat{m}_i,\hat{m}_j}$ of the pressure Eq. (10) is approximated using the Multi-Point Flux Approximation with Diamond Stencil (MPFA-D) method, originally proposed by Gao and Wu (2011), and later used by Contreras et al. (2016)), in the context of reservoir simulation, and Cavalcante et al. (2020), who extended its application to fractured porous media. The MPFA-D method is robust and consistent under full tensors and general meshes. In this scheme, the flux across each edge is given by Eq. (16):

$$(\mathcal{F}_{diff})_{\hat{m}_i,\hat{m}_j} = \tau_{IJ}^m \left(p_{\hat{m}_i} - p_{\hat{m}_j} - v_{IJ}^m \left(p_I - p_J \right) \right) \tag{16}$$

with:

$$p_I = \sum_{i=1}^{N_{neigh}} \omega_{\hat{m}_i} p_{\hat{m}_i} \tag{17}$$

$$\tau_{IJ}^m = \lambda_{IJ} \, |\overline{N}_{IJ}| \, \frac{K_{\hat{m}_i}^n K_{\hat{m}_j}^n}{K_{\hat{m}_i}^n h_{\hat{m}_j} + K_{\hat{m}_j}^n h_{\hat{m}_i}} \tag{18}$$

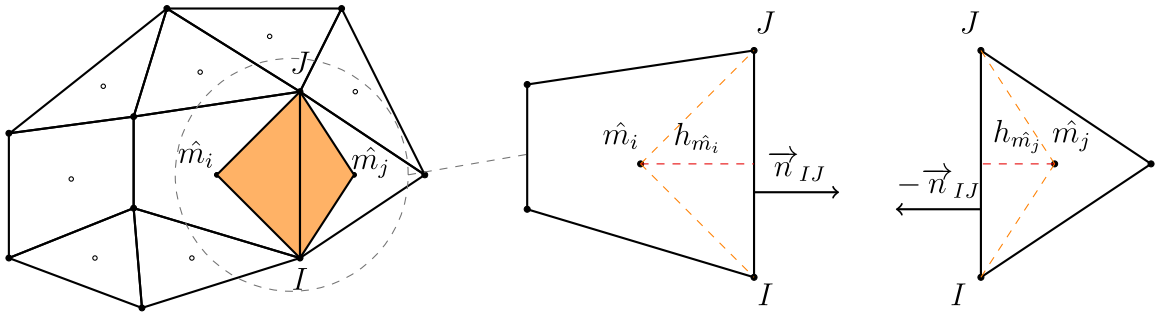

Fig. 1. Diagram of general unstructured mesh, featuring the MPFA-D diamond stencil.

$$v_{IJ}^{m} = \frac{\overrightarrow{IJ}\cdot\overrightarrow{\hat{m}_i\hat{m}_j}}{\left\|\overrightarrow{N}_{IJ}\right\|^2} - \frac{1}{\overrightarrow{N}_{IJ}}\left(\frac{K_{\hat{m}_i}^{t}}{K_{\hat{m}_i}^{n}}h_{\hat{m}_i} + \frac{K_{\hat{m}_j}^{t}}{K_{\hat{m}_j}^{n}}h_{\hat{m}_j}\right) \tag{19}$$

where τ_{IJ}, v_{IJ} and λ_{IJ} are the transmissibility, a non-dimensional tangential parameter, and face mobility, respectively. $K_{\hat{m}_i}^{n}$ is the normal projection of $\mathbf{K}_{\hat{m}_i}$ in the $\overrightarrow{N}_{IJ}$ direction, which is given by $|IJ|\vec{n}_{IJ}$, $|IJ|$ being the length of IJ. $K_{\hat{m}_i}^{t}$ is tangential projection of $\mathbf{K}_{\hat{m}_i}$ along the edge IJ. $\overrightarrow{IJ}$ is the vector connecting node I to node J and $\overrightarrow{\hat{m}_i\hat{m}_j}$ is the vector connecting the centroid of $\hat{m}_i$ to the centroid of $\hat{m}_j$. To obtain a fully cell-centered formulation, the unknowns located at the vertices in Eq. (16) must be interpolated using the cell values of the surrounding cells (except for those associated with Dirichlet boundary conditions), as shown in Eq. (17). Following Contreras et al. (2016) and Cavalcante et al. (2020), this work adopts the LPEW2 (Linear Preserving Explicit Weighting type 2) scheme proposed by Gao and Wu (2011). Since the fracture mesh is 1D, the MPFA-D reduces to the standart Two-Point Flux Approximation (TPFA):

$$(\mathcal{F}_{diff})_{\hat{f}_k^i,\hat{f}_k^j} = \tau_{IJ}^{f}\,(p_{\hat{f}_k^i} - p_{\hat{f}_k^j}) \tag{20}$$

$$\tau_{IJ}^{f} = \lambda_{IJ}\,|\overrightarrow{N}_{IJ}|\,\frac{K_{\hat{f}_k^i}^{n}K_{\hat{f}_k^j}^{n}}{K_{\hat{f}_k^i}^{n}h_{\hat{f}_k^j} + K_{\hat{f}_k^j}^{n}h_{\hat{f}_k^i}} \tag{21}$$

3.3. Neighbor advective fluxes

The matrix advective flux $(\mathcal{F}_{adv})_{\hat{m}_i,\hat{m}_j}$ and the matrix advective flux $(\mathcal{F}_{adv})_{\hat{f}_k^i,\hat{f}_k^j}$ are define as:

$$(\mathcal{F}_{adv})_{\hat{m}_i,\hat{m}_j} = (f_w)_{\hat{m}_i,\hat{m}_j}(\mathcal{F}_{diff})_{\hat{m}_i,\hat{m}_j} \tag{22}$$

$$(\mathcal{F}_{adv})_{\hat{f}_k^i,\hat{f}_k^j} = (f_w)_{\hat{f}_k^i,\hat{f}_k^j}(\mathcal{F}_{diff})_{\hat{f}_k^i,\hat{f}_k^j} \tag{23}$$

The values of $(f_w)_{\hat{m}_i,\hat{m}_j}$ and $(f_w)_{\hat{f}_k^i,\hat{f}_k^j}$ at the cells interfaces are functions of $(S_w)_{\hat{m}_i,\hat{m}_j}$ and $(S_w)_{\hat{f}_k^i,\hat{f}_k^j}$. Thus $f_w(S_w)$ is computed via the conventional First-Order Upwind (FOU) scheme in both cases (Contreras et al., 2016):

$$(S_w)_{\hat{m}_i,\hat{m}_j} = \begin{cases} (S_w)_{\hat{m}_i} & \text{if } (\mathcal{F}_{diff})_{\hat{m}_i,\hat{m}_j} \geq 0 \\ (S_w)_{\hat{m}_j} & \text{otherwise} \end{cases} \tag{24}$$

$$(S_w)_{\hat{f}_k^i,\hat{f}_k^j} = \begin{cases} (S_w)_{\hat{f}_k^i} & \text{if } (\mathcal{F}_{diff})_{\hat{f}_k^i,\hat{f}_k^j} \geq 0 \\ (S_w)_{\hat{f}_k^j}, & \text{otherwise} \end{cases} \tag{25}$$

The time step Δt is evaluated using Courant–Friedrichs–Lewy (C) stability condition:

$$\Delta t = \frac{\phi\,\Omega_m\,C}{\max\left[\left|\left(\frac{\partial f_w}{\partial S_w}\right)_{IJ}\vec{v}_{IJ}\cdot\overrightarrow{N}_{IJ}\right|\right] + \overline{Q}_w} \tag{26}$$

3.4. Continuous projection algorithm

Since matrix and fractures are on different topologies, in the EDFM, NNCs are created to capture the mass transfer between matrix and cell (Rostami et al., 2023), corresponding to the terms shown in Eqs. (14) and (15). Then, the pEDFM projects the fracture onto matrix faces, weakening matrix–matrix flux, and creating an extra NNC with the neighbor who shares the projection face (Ţene et al., 2017; Jiang and Younis, 2017). The algorithm used to determine fracture projection is crucial for the performance of the pEDFM (Rao and Liu, 2022; Rashid and Olorode, 2024). In the present work we proposed a robust algorithm to determine fracture projection, which guarantees a continuous projection, capable of dealing with cartesian and unstructured meshes, making the CpEDFM-U.

The fracture projection algorithm begins by determining the cells containing the fracture ends. Then, the matrix portion of the mesh containing embedded fractures is mapped to a weighted graph, with the graph nodes corresponding to cell nodes and graph edges representing cell faces. In this work, two weights for the graph connections were considered, which can be seen in Fig. 2, one being the angle between the cell face and the fracture segment, and the other being the distance between the cell face and the fracture line, using the centroid of each to calculate the distance. Then Dijkstra's algorithm (Dijkstra, 2022) is adopted to determine the shortest path in the graph, starting and finishing in the cell nodes closest to the fracture ends. Then the path computed is mapped back to the original mesh, where the edges crossed by the shortest path compose the faces that will receive a projection. Since the path traced from the start node to the end node is a continuous path, the resulting projection is also continuous. Different weights leads to different projections, as can be seen in Figs. 3 and 4. However, with mesh refinement they converge to the original geometry and for fine meshes the differences become negligible, as will be shown in Section 4. For a complex fracture network, the algorithm is run in each fracture independently, and the complete set of projections is given by the union of all of the independent sets of each fracture.

Along each face which received a fracture projection we weaken the connection between the neighbors $\hat{m}_i$ and $\hat{m}_j$ ($\tau_{IJ}^{m} = 0$). Then we define the standard EDFM NNCs, matrix–fracture and fracture–fracture. After that we create the additional pEDFM transmissibilities, which are matrix–fracture but in a cell which does not have the embedded cell. The full procedure can be found in the Algorithm 1.

The first weight we selected is the angle between the face segment and the fracture line, which is given by:

$$\theta_{IJ} = cos^{-1}\left(\frac{\overrightarrow{IJ}\cdot\overrightarrow{P_{start}^{f}P_{end}^{f}}}{\|\overrightarrow{IJ}\|\,\|\overrightarrow{P_{start}^{f}P_{end}^{f}}\|}\right) \tag{27}$$

where $P_{start}^{f} = (x_{start}^{f}, y_{start}^{f})$ and $P_{end}^{f} = (x_{end}^{f}, y_{end}^{f})$ are the fracture endpoints.

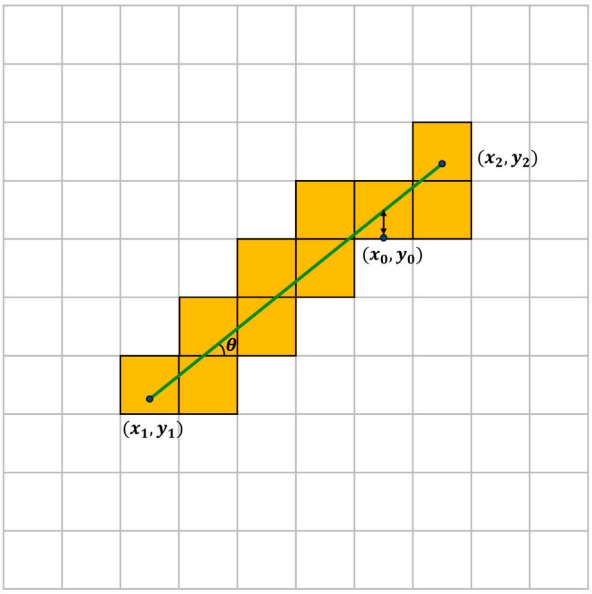

Fig. 2. Embedded cells used to create the graph and weights used.

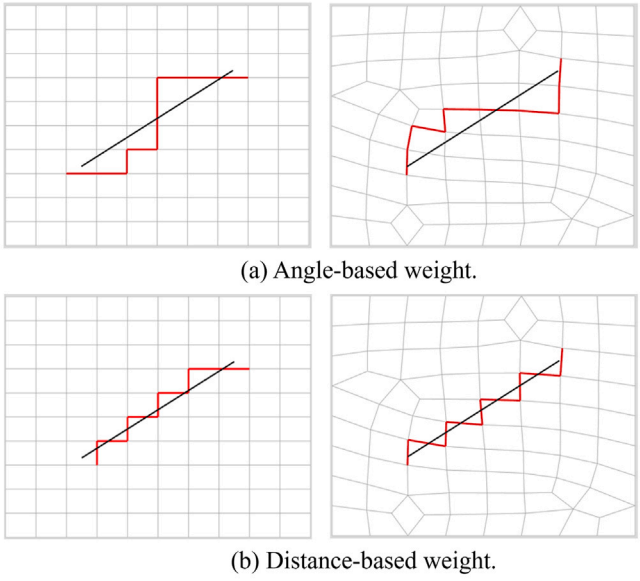

Fig. 3. Projection examples using structured and unstructured quadrilateral meshes.

The second weight we selected is given by the distance d_{IJ} from the face center, (x^m_{face}, y^m_{face}), to the fracture line, and is written as:

$$d_{IJ} = \frac{|(x^f_{end} - x^f_{start})(y^f_{start} - y^m_{face}) - (x^f_{start} - x^m_{face})(y^f_{end} - y^f_{start})|}{\sqrt{(x^f_{end} - x^f_{start})^2 + (y^f_{end} - y^f_{start})^2}} \tag{28}$$

3.4.1. Matrix–fracture flux calculation

The matrix–fracture NNC advective and diffusive fluxes between matrix cell $\hat{m}_i$ and fracture cell $\hat{f}^i_k$ can be computed similarly as their local counterparts:

$$(\mathcal{F}_{adv})_{\hat{m}_i, \hat{f}^i_k} = (f_w)_{\hat{m}_i, f_k} (\mathcal{F}_{diff})_{\hat{m}_i, \hat{f}^i_k} \tag{29}$$

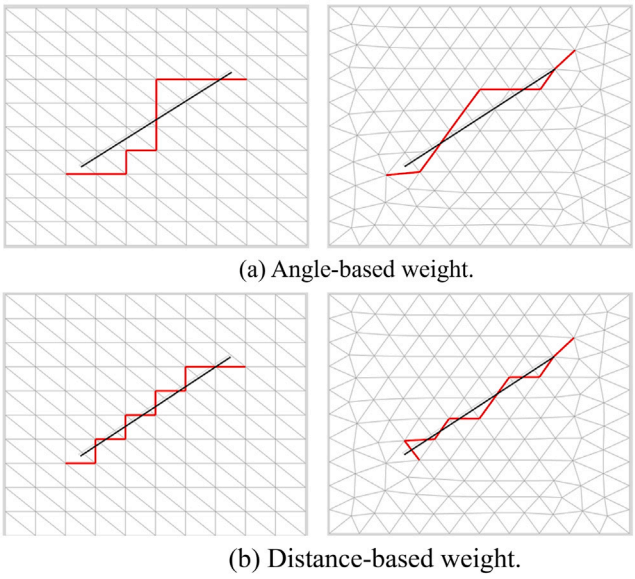

Fig. 4. Projection examples with structured and unstructured triangular meshes.

Algorithm 1 Graph-Based Continuous Fracture Projection

Require: Set of all cells with embedded fractures $\mathcal{V}_{emb}$, Set of edges of the cells with embedded fractures $\mathcal{E}_{emb}$, Set of all nodes of the cells with embedded fractures $\mathcal{N}_{emb}$, Set of all fracture geometries Ω_f
Ensure: Set of projected edges $\mathcal{E}_{proj}$

Initialization:
$\mathcal{E}_{proj} \leftarrow \emptyset$
for each fracture $\Omega_{f_k} \in \Omega_f$ **do**
  Select corresponding cells $\mathcal{V}^k_{emb} \in \mathcal{V}_{emb}$
  Select corresponding edges $\mathcal{E}^k_{emb} \in \mathcal{E}_{emb}$
  Select corresponding nodes $\mathcal{N}^k_{emb} \in \mathcal{N}_{emb}$
  ▷ **Step 1: Graph Construction**
  Construct Graph $\mathcal{G}_k = (N_k, L_k, W_k)$
  $N_k \leftarrow \mathcal{N}^k_{emb}$ ▷ Mesh nodes are mapped to graph nodes
  $L_k \leftarrow \emptyset$ ▷ Set of nodes links
  $W_k \leftarrow \emptyset$ ▷ Set of links weights
  for each face $e_k \in \mathcal{E}_{emb}$ **do**
    Identify vertices I, J sharing face e_k, add connection l_{IJ} to L_k and associate edge ID k with link l_{IJ}
  end for
  ▷ **Step 2: Weight Assignment**
  for each link $l_{IJ} \in L_k$ **do**
    Compute corresponding weight w_{IJ}
    $W_k \leftarrow w_{IJ}$
  end for
  ▷ **Step 3: Pathfinding**
  Select nodes closest to fracture tips
  $n_{start} \leftarrow \text{argmin}_{n \in N_k} \|X_n - \Omega_{f_k, start}\|$
  $n_{end} \leftarrow \text{argmin}_{n \in N_k} \|X_n - \Omega_{f_k, end}\|$
  $\mathcal{P}_{nodes} \leftarrow \text{Dijkstra}(\mathcal{G}_k, n_{start}, n_{end})$
  ▷ **Step 4: Projection Mapping**
  $\mathcal{E}^k_{proj} \leftarrow \emptyset$
  for each consecutive pair (u, v) in $\mathcal{P}_{nodes}$ **do**
    Retrieve face ID k associated with link l_{uv}
    Add e_k to $\mathcal{E}^k_{proj}$
  end for
  $\mathcal{E}_{proj} \leftarrow \mathcal{E}_{proj} \cup \mathcal{E}^k_{proj}$
end for
return $\mathcal{E}_{proj}$

where $f_w(S_w)$ is again computed via the FOU scheme:

$$(S_w)_{\hat{m}_i,\hat{f}_k^i} = \begin{cases} (S_w)_{\hat{m}_i} & \text{if } (\mathcal{F}_{diff})_{\hat{m}_i,\hat{f}_k^i} \geq 0 \\ (S_w)_{f_k} & \text{otherwise} \end{cases} \tag{30}$$

and:

$$(\mathcal{F}_{diff})_{\hat{m}_i,\hat{f}_k^i} = (\lambda)_{\hat{m}_i,\hat{f}_k^i} T_{\hat{m}_i,\hat{f}_k^i} \left(p_{\hat{m}_i} - p_{\hat{f}_k^i} \right) \tag{31}$$

where $(\lambda)_{\hat{m}_i,\hat{f}_k^i} = ((\lambda)_{\hat{m}_i} + (\lambda)_{\hat{f}_k^i})/2$ and:

$$T_{\hat{m}_i,\hat{f}_k^i} = K_{\hat{m}_i,\hat{f}_k^i} \frac{A_{\hat{f}_k^i}}{\langle d_{\hat{m}_i,\hat{f}_k^i} \rangle}, \; K_{\hat{m}_i,\hat{f}_k^i} = \frac{A_{\hat{m}_i} K_{\hat{m}_i} + L_{\hat{f}_k^i} K_{\hat{f}_k^i}}{\left(A_{\hat{m}_i} + L_{\hat{f}_k^i} \right) K_{\hat{m}_i} K_{\hat{f}_k^i}} \tag{32}$$

where $A_{\hat{f}_k^i}$ is the area of the segment embedded, $A_{\hat{m}_i}$ is the matrix cell area and $L_{\hat{f}_k^i}$ is the fracture cell length. $\langle d_{\hat{m}_i,\hat{f}_k^i} \rangle$ is the average distance between the cell and the embedded fracture segment which is given by:

$$\langle d_{\hat{m}_i,\hat{f}_k^i} \rangle = \frac{1}{|\Omega_{\hat{m}_i}|} \int_{\Omega_{\hat{m}_i}} d_{\hat{m}_i,\hat{f}_k^i} \, d\Omega_{\hat{m}_i} \tag{33}$$

where $d_{\hat{m}_i,\hat{f}_k^i}$ is the distance from a point inside the matrix cell to the fracture segment.

Furthermore, the $(\mathcal{F}_{diff})_{\hat{m}_j,\hat{f}_k^i}$ between the fracture cell $\hat{f}_k^i$ and the projection neighbor $\hat{m}_j$ is defined as:

$$(\mathcal{F}_{diff})_{\hat{m}_j,\hat{f}_k^i} = (\lambda)_{\hat{m}_j,\hat{f}_k^i} T_{\hat{m}_j,\hat{f}_k^i} \left(p_{\hat{m}_j} - p_{\hat{f}_k^i} \right) \tag{34}$$

where $(\lambda)_{\hat{m}_j,\hat{f}_k^i} = ((\lambda)_{\hat{m}_j} + (\lambda)_{\hat{f}_k^i})/2$ and:

$$T_{\hat{m}_j,\hat{f}_k^i} = K_{\hat{m}_j,\hat{f}_k^i} \frac{A_{\hat{f}_k^i}^{proj}}{\langle d_{\hat{m}_j,\hat{f}_k^i} \rangle}, \; K_{\hat{m}_j,\hat{f}_k^i} = \frac{A_{\hat{m}_j} K_{\hat{m}_j} + L_{\hat{f}_k^i} K_{\hat{f}_k^i}}{\left(A_{\hat{m}_j} + L_{\hat{f}_k^i} \right) K_{\hat{m}_j} K_{\hat{f}_k^i}} \tag{35}$$

where $A_{\hat{f}_k^i}^{proj}$ is the cell $\hat{f}_k^i$ projected area, and $\langle d_{\hat{m}_j,\hat{f}_k^i} \rangle$ is the distance between the cells $\hat{m}_j$ and $\hat{f}_k^i$ centroids.

3.4.2. Fracture–fracture flux calculation

The fracture–fracture NNC fluxes between cell $\hat{f}_k^i$ in the fracture f_k and cell $\hat{f}_l^i$ in the fracture f_l are computed as:

$$(\mathcal{F}_{adv})_{\hat{f}_k^i,\hat{f}_l^i} = (f_w)_{\hat{f}_k^i,\hat{f}_l^i} (\mathcal{F}_{diff})_{\hat{f}_k^i,\hat{f}_l^i} \tag{36}$$

where:

$$(S_w)_{\hat{f}_k^i,\hat{f}_l^i} = \begin{cases} (S_w)_{\hat{f}_k^i} & \text{if } (\mathcal{F}_{diff})_{\hat{f}_k^i,\hat{f}_l^i} \geq 0 \\ (S_w)_{\hat{f}_l^i} & \text{otherwise} \end{cases} \tag{37}$$

and:

$$(\mathcal{F}_{diff})_{\hat{f}_k^i,\hat{f}_l^i} = (\lambda)_{\hat{f}_k^i,\hat{f}_l^i} T_{\hat{f}_k^i,\hat{f}_l^i} \left(p_{\hat{f}_k^i} - p_{\hat{f}_l^i} \right) \tag{38}$$

where $(\lambda)_{\hat{f}_k^i,\hat{f}_l^i} = ((\lambda)_{\hat{f}_k^i} + (\lambda)_{\hat{f}_l^i})/2$. $T_{\hat{f}_k^i,\hat{f}_l^i}$ which is computed via the 'star-delta' transformation of the intersecting fracture cells $\hat{f}_k^i$ and $\hat{f}_l^i$ (Karimi-Fard et al., 2004).

4. Results

This section presents the results obtained from three different model problems, each highlighting the capabilities and limitations of the compared methods. Example 1 involves a single-phase simulation in a reservoir with a diagonal sealing fracture, comparing the performance of the EDFM, pEDFM, and CpEDFM-U methods across different resolutions of structured and unstructured grids. The goal is to demonstrate that the CpEDFM-U effectively handles all mesh resolutions, ensuring an accurate representation of flow behavior, which is demonstrated using the relative L2 norm, globally weighted by volume, of the error between the pressure fields obtained using CpEDFM-U and the reference solution obtained using the MRST considering a refined conformed DFM solution. Example 2 presents a two-phase flow simulation in a square reservoir with an inclined fracture, using a simulation time up to 1.1 PVI (Pore Volume Injected). This example aims to highlight the performance differences between the EDFM, pEDFM, and CpEDFM-U methods. Once again, the same L2 norm of error is adopted to compare the different solutions against the MRST reference solution and the cumulative oil production curves are compared. Example 3 explores a two-phase flow simulation with 30 fractures (flow channels and barriers, with random angles and locations within the domain), aiming to demonstrate the CpEDFM-U formulation ability to handle complex scenarios accurately, particularly in irregular geometries involving sealing fractures.

4.1. Single-phase flow in a reservoir with a diagonal barrier

In this example, we show the limitations of the original pEDFM method in modeling inclined fractures with low conductivity by comparing its performance against our CpEDFM-U method. The focus is on the differences between the fracture projection criteria adopted by each approach and the impacts of these differences on the continuity of projections and the accuracy of the pressure field. Additionally, it is important to highlight the limitation of the EDFM, which is unable to adequately represent sealing fractures. In Fig. 5, we present a structured quadrilateral mesh (8 × 4) containing a diagonal fracture (in green) and its projections onto the faces of the cells in the x-direction (red lines) and y-direction (blue lines). In Fig. 5a, the projections of the pEDFM are presented, which is built locally, that is, in each intersected cell independently, following the projection criterion of Jiang and Younis (2017). Fig. 5b (angle-based weighting) and 5c (distance-based weighting) show the projections using the CpEDFM-U, developed in this work, which uses an alternative graph-based criterion to ensure the continuity of the projections.

Fig. 5a highlights the presence of discontinuities in the fracture projections, indicated by the light blue arrow. These discontinuities create artificial flow paths through a fracture that, in theory, should be impermeable, with near-zero conductivity, which represents a significant modeling error. Unlike pEDFM, the graph-based CpEDFM-U projections in Figs. 5b and 5c are, by definition, connected structures, ensuring continuous projection along the entire extent of the fracture, even for inclined geometries, on arbitrary 2D meshes, and using the weighting criteria applied in this work. To investigate the impacts of the limitations of pEDFM in simulating inclined sealing fractures, especially the errors associated with the holes generated by projection discontinuities, and to demonstrate that CpEDFM-U can represent these fractures continuously and more accurately, one-phase flow simulations were conducted, considering an impermeable diagonal fracture that completely crosses a rectangular domain (10 × 5 meters), dividing the reservoir into two distinct regions, schematically presented in Fig. 6. This Figure presents an 8 × 4 structured quadrilateral mesh as well as the fracture location. In all simulations, boundary conditions were applied with a prescribed pressure of 1 bar on the left face, 0 bar on the right face, and zero flux on the upper and lower faces of the domain. Six simulations were performed, comparing structured quadrilateral meshes and unstructured triangular meshes with resolutions of: 8 × 4, 40 × 20 and 200 × 100.

The main objective was to compare the pressure fields obtained by the EDFM, pEDFM, and CpEDFM-U methods (using both types of weights) with a reference solution, which was obtained from an unstructured triangular mesh with 18,970 control volumes, adapted to the fracture geometry. This mesh was generated using the Gmsh software (see Fig. 7) and features progressive refinement around the fracture. Near the fracture, a reduced element size was adopted to align the mesh cell faces with the fracture line, while larger elements were used at the domain boundaries to increase the accuracy in capturing the hydraulic blockage effects imposed by the low-conductivity inclined fracture.

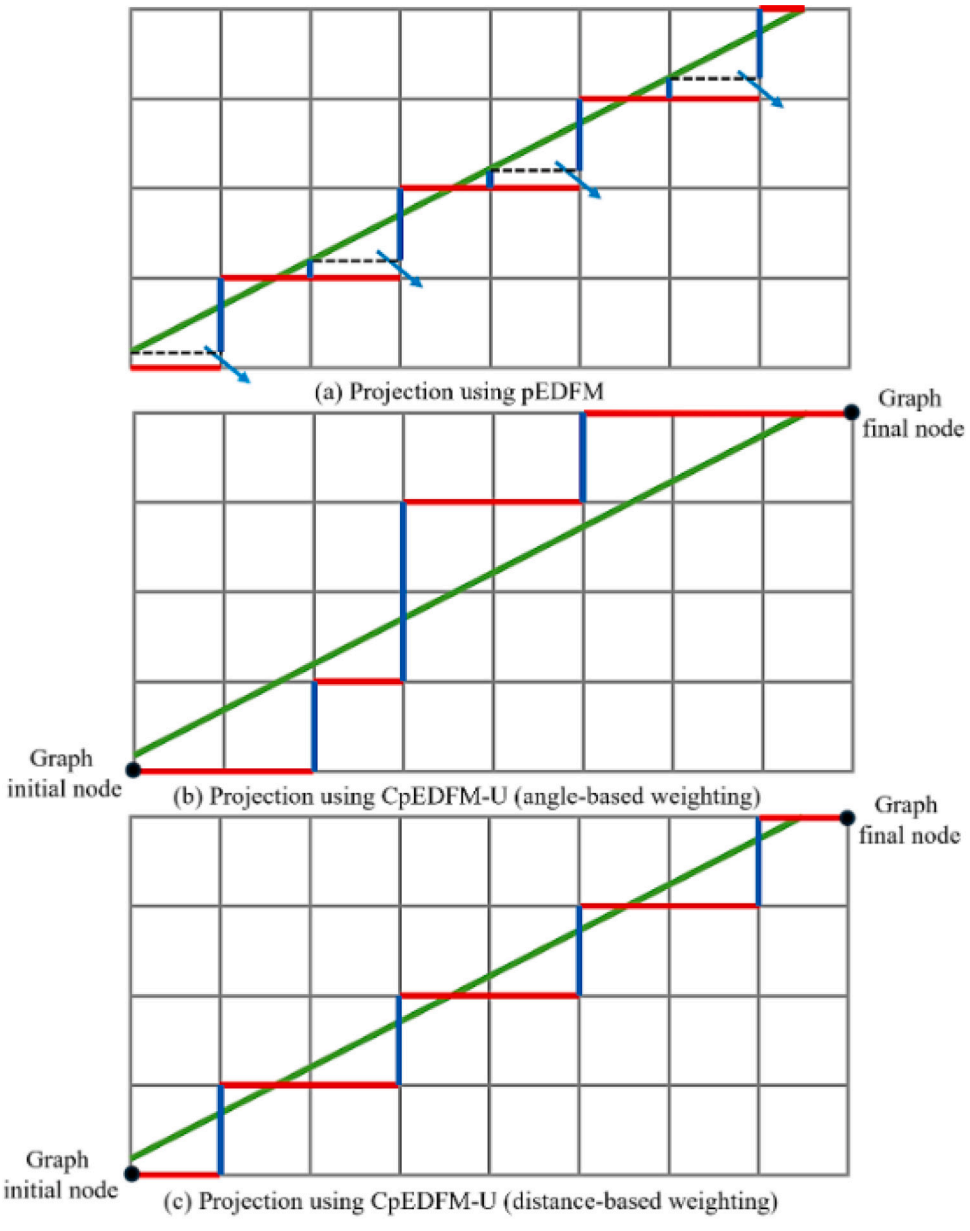

Fig. 5. Single-Phase Flow in a Reservoir with a Diagonal Barrier. Comparison between the projections of a diagonal fracture: (a) using the pEDFM method; (b) CpEDFM-U, angle-based weighting and (c) CpEDFM-U, distance-based weighting.

This discretization process allows for the direct simulation of the fracture's influence on flow, without the need to resort to Projection-based methods such as pEDFM or CpEDFM-U. The simulation was conducted using the MRST (MATLAB Reservoir Simulation Toolbox) with the DFM module formulation (Karimi-Fard et al., 2004; Sandve et al., 2012), which also utilizes multiple-point flow approximations. This configuration enabled the calculation of a more precise and physically representative pressure field, providing a reliable basis for evaluating the results obtained with embedded fracture models.

The input parameters for the simulation model analyzed in this section are summarized in Table 1.

Figs. 8 and 9 present the pressure fields obtained with the different embedded fracture methods using an 8 × 4 structured quadrilateral mesh (Fig. 8) and an unstructured triangular mesh with 84 CVs (Fig. 9). The pressure field obtained using EDFM is shown in Figs. 8a and 9a, the solution generated with pEDFM is shown in Figs. 8b and 9b, and Figs. 8c, 9c,8d, and 9d display the results obtained with the CpEDFM-U method using, respectively, the angle-based weighting criterion (c) and the distance-based weighting criterion (d). Finally, Figs. 8e and 9e present the reference solution obtained with the high-resolution DFM mesh.

Table 1
Single-Phase Flow in a Reservoir with a Diagonal Barrier: Model parameters.

Input Data	Value	Unit
Reservoir dimension	[10, 5]	m
Matrix porosity	0.3	–
Matrix permeability	10^{-3}	darcys
Fracture porosity	0.01	–
Fracture permeability	10^{-9}	darcys
Fracture aperture	0.05	m

It can be observed in Figs. 8 and 9a that the EDFM completely ignores the presence of the barrier and shows a linear pressure distribution. The pEDFM solution (8b and 9b) allows pressure communication throughout the fracture, reflecting the discontinuities that appear by

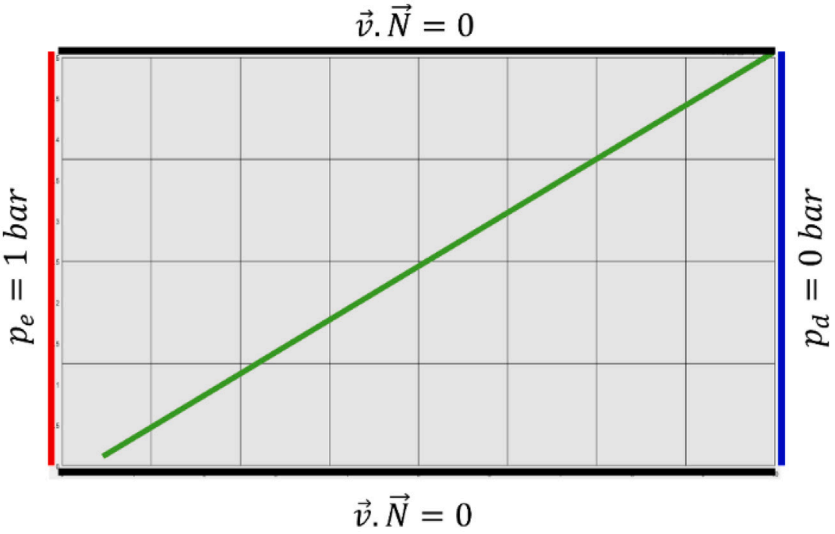

Fig. 6. Single-Phase Flow in a Reservoir with a Diagonal Barrier: Problem configuration with fracture position and boundary conditions, and discrete mesh with 32 structured quadrilateral CVs.

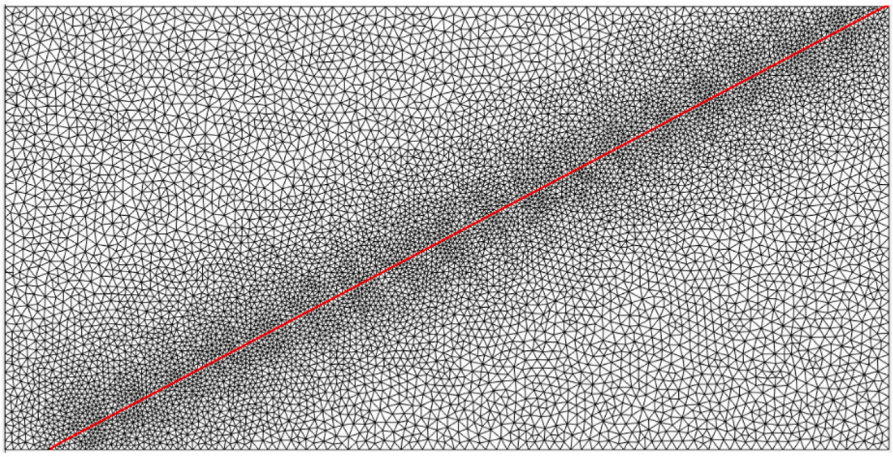

Fig. 7. Single-Phase Flow in a Reservoir with a Diagonal Barrier: Conforming DFM mesh (18.970 CVs) used to obtain a reference solution.

the local projection criterion proposed by Jiang and Younis (2017), for inclined fractures with respect to the mesh. In contrast, the pressure field generated with the DFM (Figs. 8e and 9e) shows a strong contrast between the two sides of the fracture, highlighting its role as a flow barrier. Since pressures are prescribed on the left and right boundaries of the domain, the sealing fracture prevents hydraulic communication between the two sides, resulting in a sharp pressure difference. Figs. 8c and 9c, and Figs. 8d and 9d show that the pressure fields obtained with CpEDFM-U closely resemble the reference solution. For those meshes, with 32 and 84 CVs, and fracture configuration, the distance-based criterion (Figures 8d and 9d) aligns more directly with the fracture geometry, and both criteria guarantee the continuity of the projection, avoiding artifacts observed in the EDFM and pEDFM solutions. Figs. 10 and 11 present, respectively, the pressure fields for the structured quadrilateral mesh with 800 control volumes and for the unstructured triangular mesh with 1868 control volumes. Figs. 10a and 11a show the solution using EDFM, Figs. 10b and 11b present the solution generated with pEDFM, while Figs. 10c and 11c, and 10d and 11d present the results from CpEDFM-U using angle-based (ABW) and distance-based (DBW) weights, respectively. Figs. 10e and 11e show the reference solution obtained with the DFM mesh. As the mesh is refined, both CpEDFM-U criteria increasingly align with the actual fracture geometry, enhancing the representation of the flow barrier. This improvement leads to continuous projections that converge to the real fracture geometry as the mesh is refined.

The last two single-phase simulations were performed with two different meshes, a structured quadrilateral mesh with 20,000 control volumes (Fig. 12) and an unstructured triangular mesh with 46,458 control volumes 13, as in the previous simulations. This simulation shows that as the mesh resolution increases, the projections of CpEDFM-U using both weights tend to align more closely with the real geometry of the fracture, as observed in Figs. 12 and 13 (angle-based weight (c) and distance-based weight (d). The pressure fields of the EDFM (Figs. 12a and 13a), pEDFM (Figs. 12b and 13b), and the DFM solution (Figs. 12e and 13e) are also presented.

Table 2 presents the error values in the pressure fields of the embedded fracture methods (i.e, EDFM, pEDFM and CpEDFM-U) compared to the reference solution, measured by the L2 norm globally weighted by volume (Kim, 2017). This norm is a mathematical measure used to quantify the difference between two solutions, typically a reference solution obtained on a finer mesh and an approximate solution obtained on a coarser mesh. The idea is to calculate the mean squared error between the two solutions, weighing each term by the volume V_i of the corresponding cell, so that larger cells, which represent more significant regions of the reservoir, have a greater influence on the final value. This measure is called “global” because it considers the entire domain

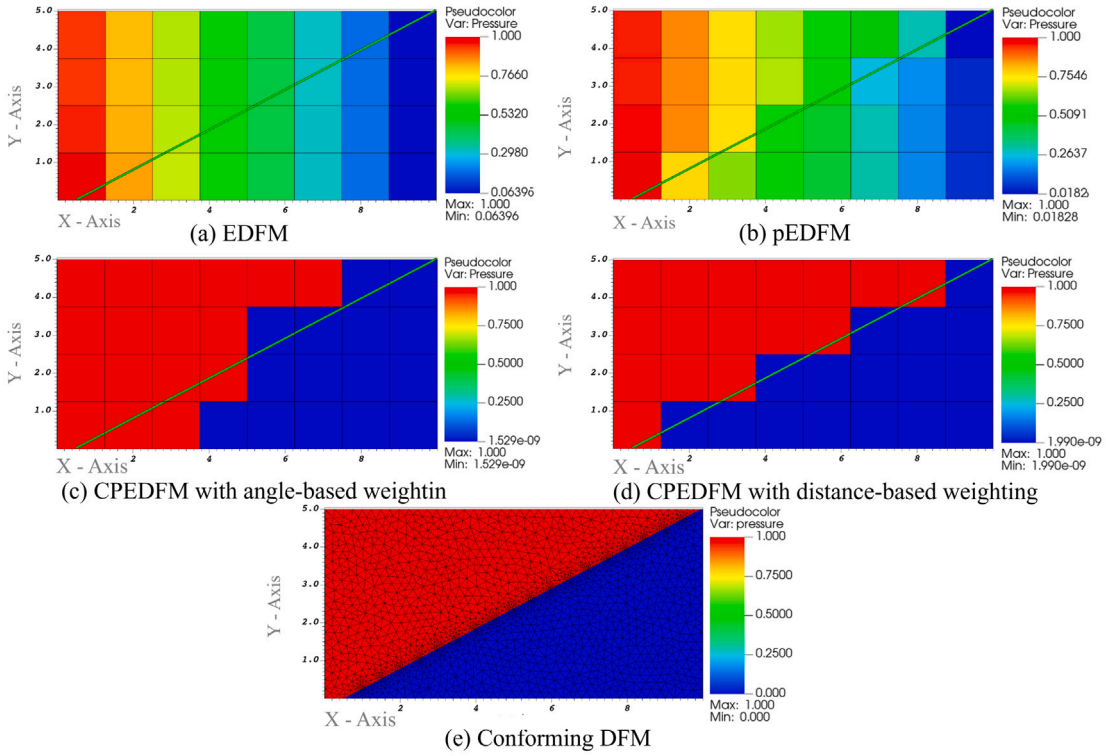

Fig. 8. Single-Phase Flow in a Reservoir with a Diagonal Barrier: Pressure fields with the structured quadrilateral mesh with 32 CVs for different fracture representation. (a) EDFM; (b) pEDFM; (c) CpEDFM-U with ABW; CpEDFM-U with DBW; (e) Conforming DFM.

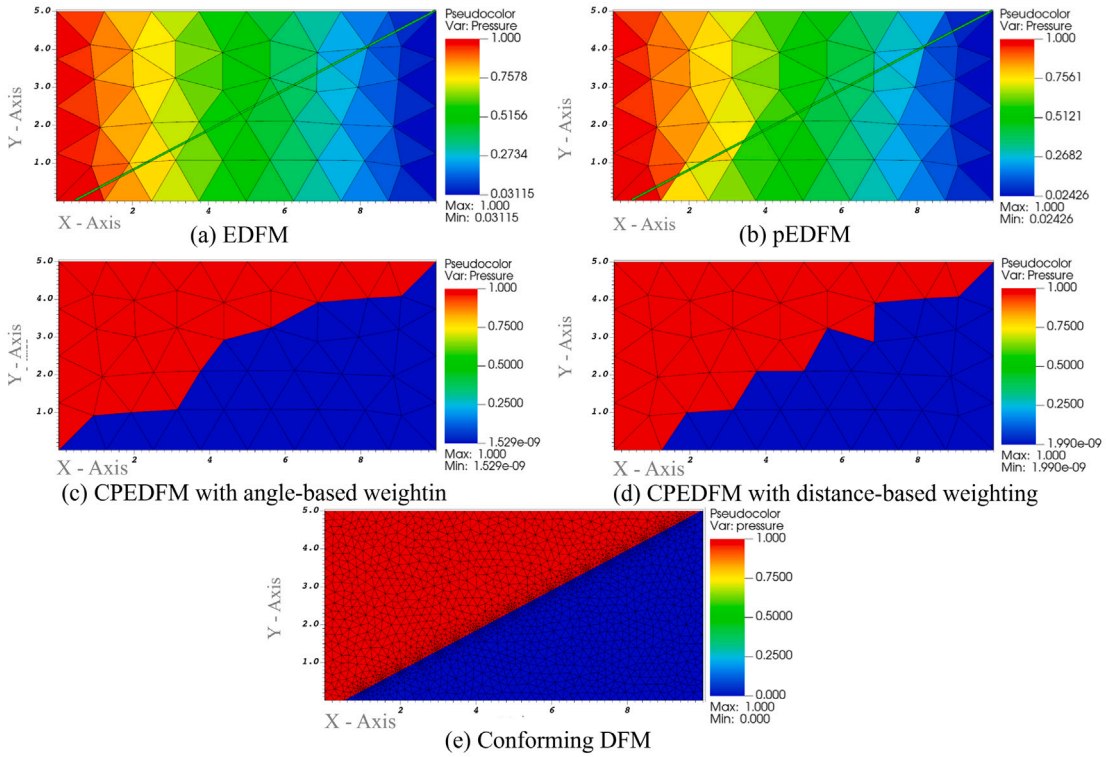

Fig. 9. Single-Phase Flow in a Reservoir with a Diagonal Barrier: Pressure fields with the unstructured triangular mesh with 84 CVs for different fracture representation. (a) EDFM; (b) pEDFM; (c) CpEDFM-U with ABW; CpEDFM-U with DBW; (e) Conforming DFM.

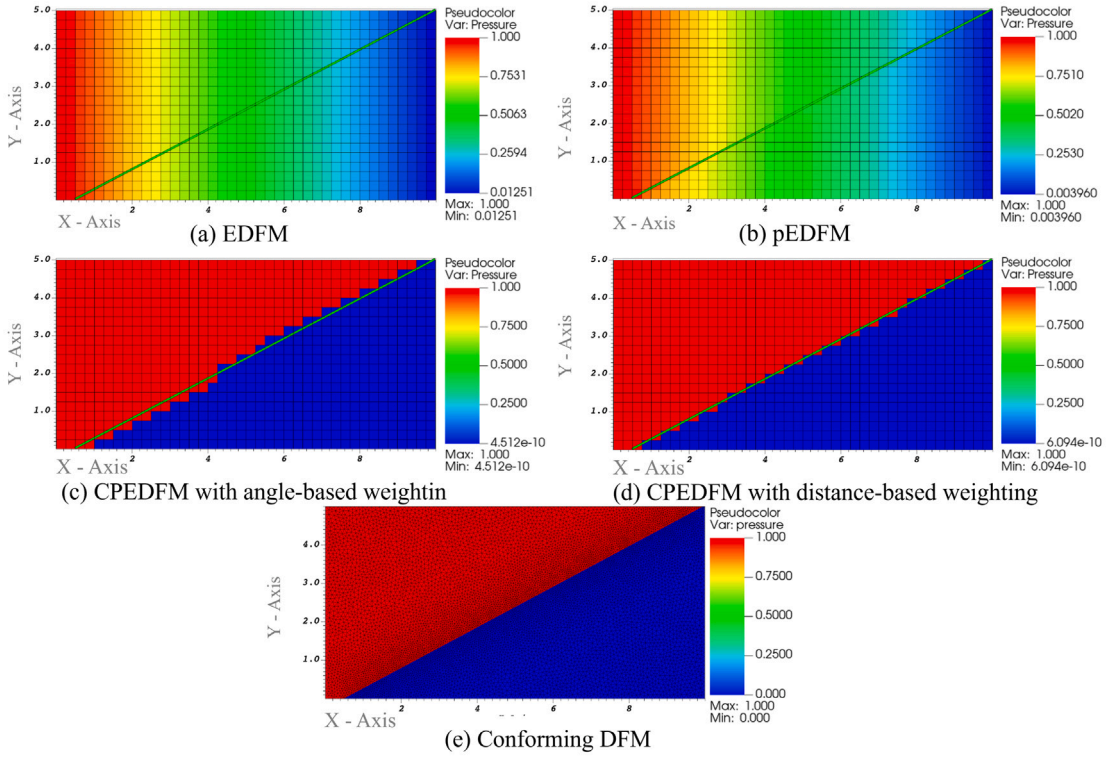

Fig. 10. Single-Phase Flow in a Reservoir with a Diagonal Barrier: Pressure fields with **the structured quadrilateral mesh with 800 CVs** for different fracture representation. (a) EDFM; (b) pEDFM; (c) CpEDFM-U with ABW; CpEDFM-U with DBW; (e) Conforming DFM.

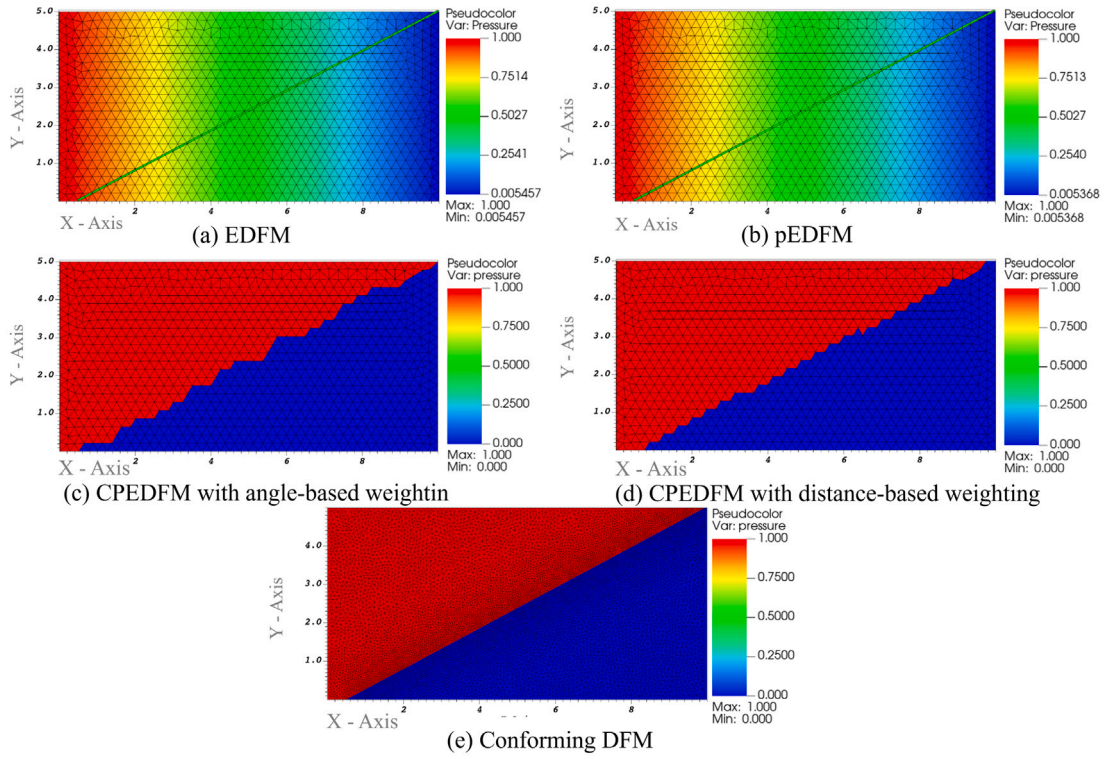

Fig. 11. Single-Phase Flow in a Reservoir with a Diagonal Barrier: Pressure fields with the **1,868 CVs unstructured triangular mesh** for different fracture representation. (a) EDFM; (b) pEDFM; (c) CpEDFM-U with ABW; CpEDFM-U with DBW; (e) Conforming DFM.

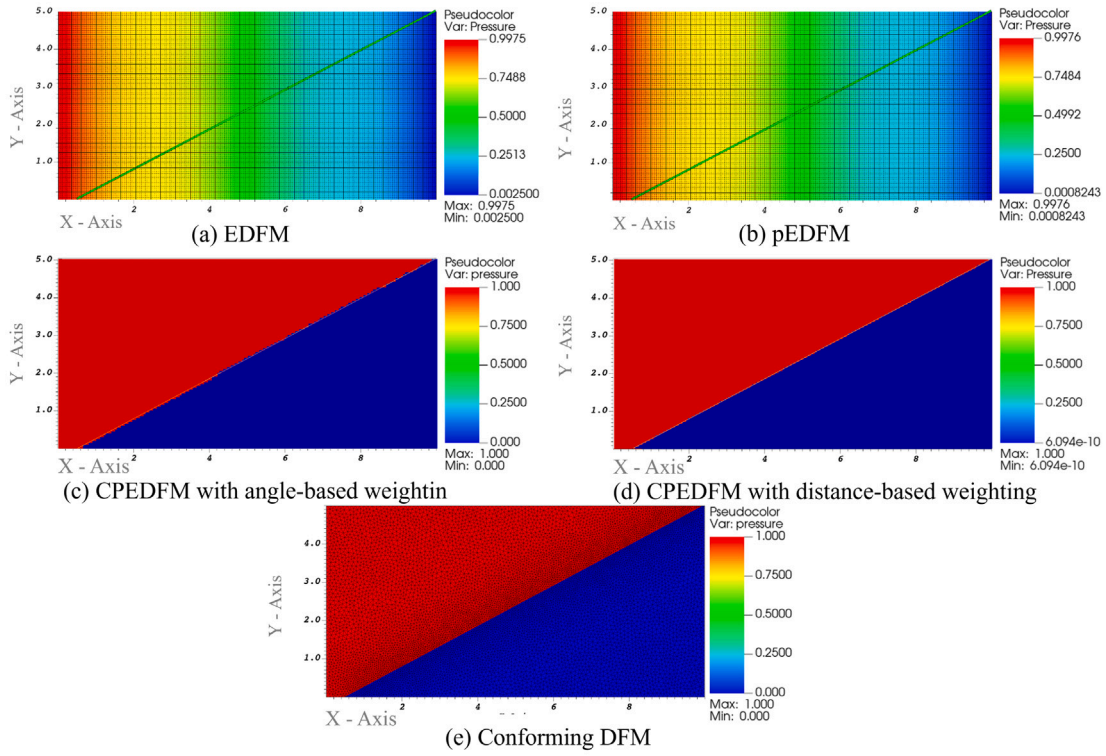

Fig. 12. Single-Phase Flow in a Reservoir with a Diagonal Barrier: Pressure fields with the **structured quadrilateral mesh with 20,000 CVs** for different fracture representation. (a) EDFM; (b) pEDFM; (c) CpEDFM-U with ABW; CpEDFM-U with DBW; (e) Conforming DFM.

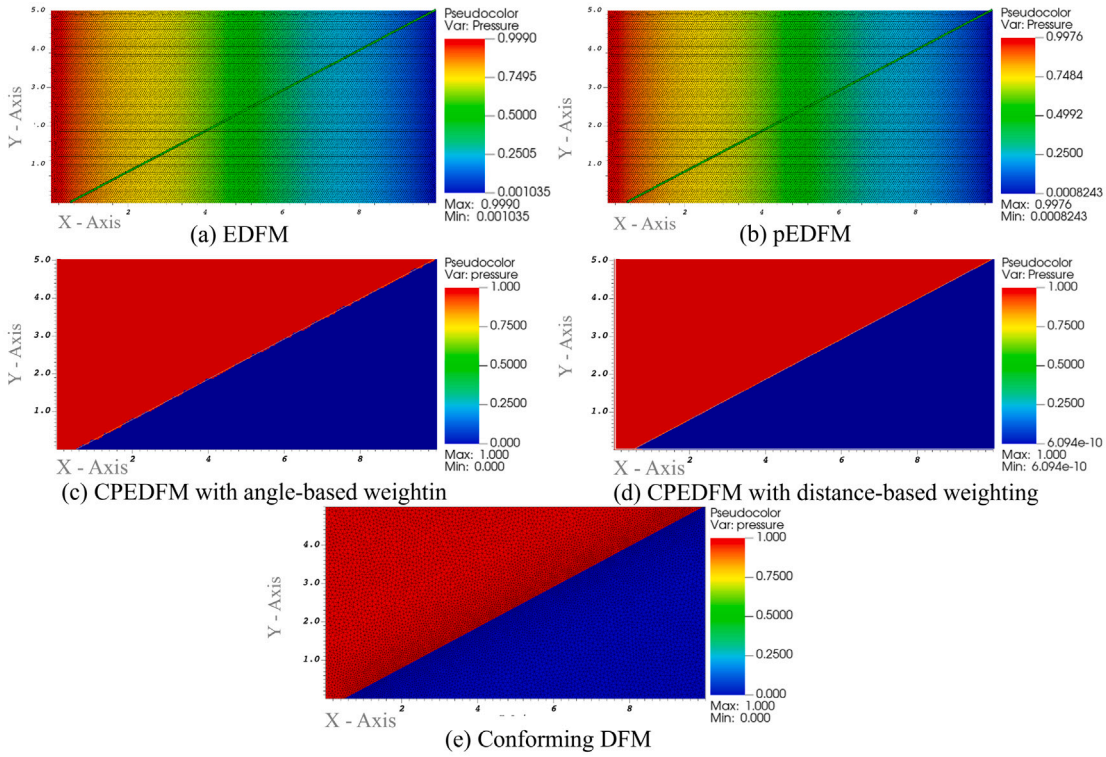

Fig. 13. Single-Phase Flow in a Reservoir with a Diagonal Barrier: Pressure fields with the **46,458 CVs unstructured triangular mesh** for different fracture representation. (a) EDFM; (b) pEDFM; (c) CpEDFM-U with ABW; CpEDFM-U with DBW; (e) Conforming DFM.

Table 2
Comparison of EDFM, pEDFM, and CpEDFM-U results for different grid types and control volumes (CVs).

CVs	Type	EDFM	**pEDFM**	CpEDFM-U (angle)	CpEDFM-U (distance)
32	Structured quadrilateral	0.56059	0.49007	0.075473	0.05318
84	Unstructured triangular	0.54494	0.51519	0.06226	0.03191
800	Structured quadrilateral	0.54374	0.52295	0.054177	0.050278
1868	Unstructured triangular	0.54341	0.53489	0.056265	0.05567
20000	Structured quadrilateral	0.54025	0.5359	0.053572	0.049986
46458	Unstructured triangular	0.53226	0.53414	0.05349	0.05013

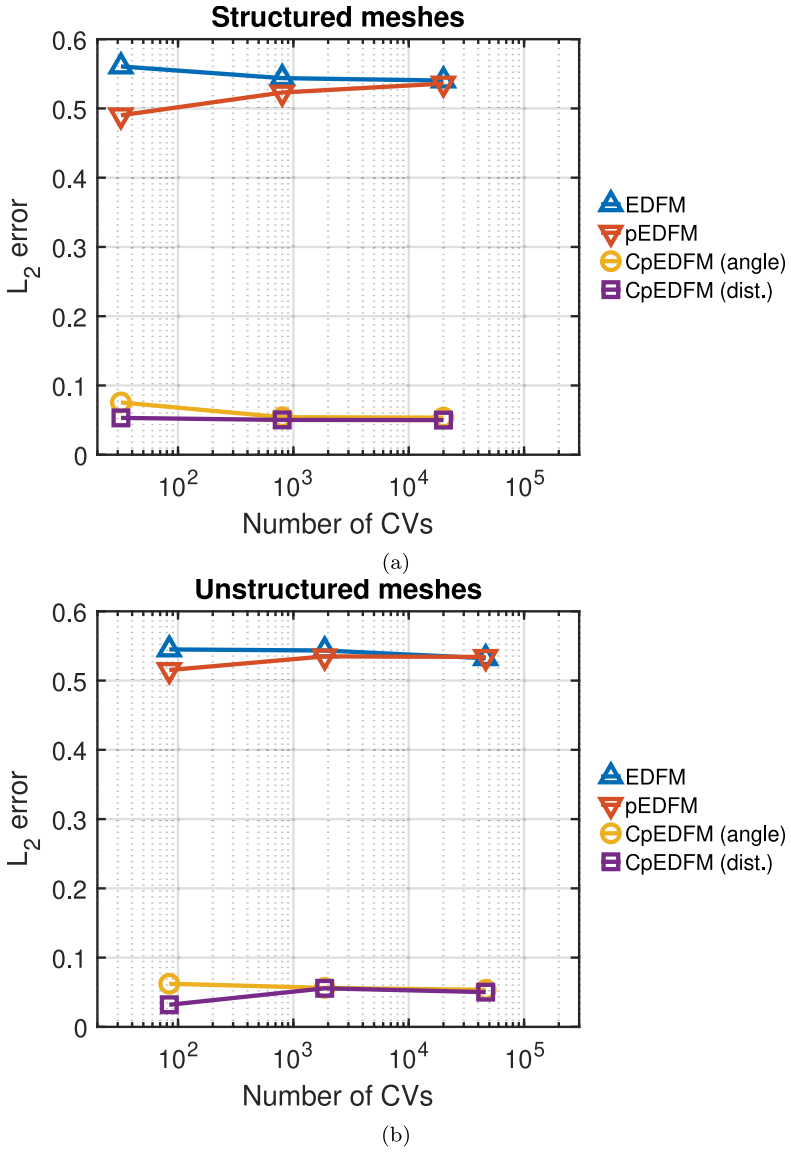

Fig. 14. L_2 error versus number of CVs. (a) Structured meshes: 32, 800 and 20000 CVs. (b) Unstructured meshes: 84, 1868 and 46458 CVs.

in a single metric and is independent of the number of points, as the solutions do not need to have the same number of cells. It is enough to project the reference solution onto the points of the approximate mesh (via interpolation) before the calculation. The formula for this norm is given by:

$$E_{L2} = \frac{\sqrt{\sum_{i=1}^{N} V_i \left(p_i^{approx} - p_i^{ref}\right)^2}}{\sqrt{\sum_{i=1}^{N} V_i \left(p_i^{ref}\right)^2}} \tag{39}$$

where N is the number of cells in the mesh used for the approximate solution, Vi is the volume of cell i, piapprox is the pressure obtained in the approximate solution, and piref is the pressure of the reference solution. The results show that the CpEDFM-U method consistently performs better than both EDFM and pEDFM, with significantly lower errors across all mesh resolutions. For the mesh lower resolution using a structured quadrilateral mesh with 32 control volumes, the CpEDFM-U method achieves an error close to 0.05, while EDFM and pEDFM exhibit considerably higher errors. We achieve high accuracy using CpEDFM-U even with coarser meshes and as the mesh resolution increases the errors remain very low, being even slightly smaller using distance-based weight. In contrast, the errors of EDFM and pEDFM are two-order of magnitude higher, and do not show any improvement with mesh refinement. Additionally, Fig. 14 presents the L_2 error as a function

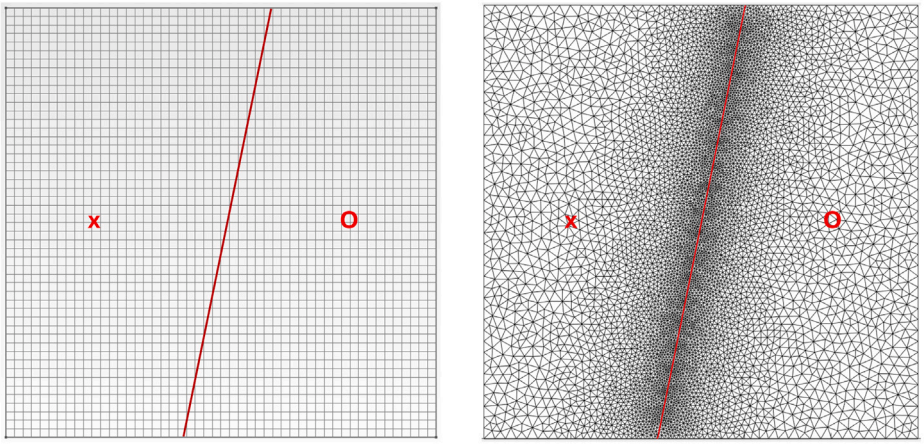

(a) Mesh used for the EDFM, pEDFM, and CPEDFM-U simulations.

(b) Unstructured grid conforming to the fracture (DFM).

Fig. 15. Two-phase Flow in a Square Reservoir with Two Wells and an Inclined Barrier: Quadrilateral structured mesh with 2500 control volumes and triangular unstructured mesh with 13,664 control volumes.

of the number of control volumes (CVs) for different numerical approaches using 14(a) structured meshes and 14(b) unstructured meshes. The classical EDFM and pEDFM exhibit relatively high errors, on the order of 10^{-1}, which remain nearly constant with mesh refinement. In contrast, both CpEDFM formulations (angle-based and distance-based) show significantly lower errors, around 10^{-2}, representing an improvement of approximately one order of magnitude. Moreover, the error remains consistently low as the number of CVs increases, highlighting the robustness of CpEDFM on unstructured meshes.

These results highlight that the local projection criterion of pEDFM can compromise the accuracy of the simulation, especially in cases of inclined low-conductivity fractures, as observed by Rashid and Olorode (2023). The discontinuities introduced in the projections allow for improper fluid leakage, even in impermeable fractures, directly affecting the model's response. The CpEDFM-U developed in this work ensures a globally connected projection, eliminating discontinuities and providing greater physical fidelity in modeling of inclined fractures. Thus, for cases where accurate representation of the flow barrier is essential, CpEDFM-U proves to be a more robust and reliable alternative to the classical pEDFM.

4.2. Two-phase flow in a square reservoir with an inclined barrier

To further highlight the impacts of the discontinuities in pEDFM projections on cumulative oil production curves, a two-phase (water/oil) simulation was performed in a fractured reservoir. The primary objective is to demonstrate the accuracy of the CpEDFM-U model compared to the EDFM and pEDFM models, using as a benchmark a reference solution with a conforming DFM grid (simulated in MRST — MATLAB Reservoir Simulation Toolbox). This reference solution precisely matches the fracture geometry and location, ensuring that the fracture line aligns with the rock matrix mesh control volume faces. This analysis is crucial for verifying CpEDFM-U ability to more faithfully represent flow behavior in reservoirs with sealing fractures and arbitrary fracture orientations. The reservoir consists of a square domain with 100 m × 100 m. A diagonal sealing fracture divides the reservoir into two parts. The inclined fracture orientation was intentionally chosen to generate multiple connectivity discontinuities in pEDFM projections, thereby emphasizing CpEDFM-U methods capability to maintain projection continuity regardless of fracture orientation. In this problem, for the EDFM, pEDFM, and CpEDFM-U methods, we have used a structured quadrilateral mesh with 2500 control volumes. In contrast, the reference solution is obtained from a conforming DFM formulation with 5640 control volumes, ensuring geometric conformity with the fracture and allowing its influence to be simulated directly — without relying on projection methods like EDFM, pEDFM or CpEDFM-U. This approach provides a more accurate representation of the structural heterogeneity of the medium. The simulation time is up to 1.1 PVI (Pore Volume Injection), which is the time dimensionless by the reservoir pore volume, representing how many fluid volumes have been injected into the porous medium (Lake et al., 2014). The wells are positioned to create flow perpendicular to the fracture: a water injector is placed on the left side of the domain, approximately at the midpoint of the y-axis, while the oil producer is symmetrically located on the right side. This configuration enhances the observation of the sealing fracture's effects on fluid propagation and model performance. In the simulation, zero flux was considered on all faces of the domain. Table 3 summarizes the key simulation data, including rock and fluid properties, as well as operational parameters.

Table 3
Two-phase Flow in a Square Reservoir with Two Wells and an Inclined Barrier: Input data.

Input Parameter	Value	Unit
Domain dimensions	[100, 100]	m
Matrix porosity	0.1	–
Matrix permeability	10^{-3}	darcys
Fracture porosity	0.4	–
Fracture permeability	10^{-12}	darcys
Fracture aperture	0.01	m
Water viscosity	1.0	cP
Oil viscosity	1.0	cP
Injector well pressure	1	–
Time simulation	1.1	PVI
Initial saturation	[0, 1]	–

Fig. 15 shows the meshes configurations used in the different models, along with the injector well (marked with "X") and producer well (marked with "O"). The inclined fracture crossing the domain is clearly visible, as is the difference in grid resolution adopted by the EDFM, pEDFM, and CpEDFM-U models 15a and that used for the reference solution 14b.

Fig. 16 compares the resulting pressure fields at the end of the simulation. The EDFM model 16a completely ignores the sealing fracture, showing a pressure field that gradually declines throughout the reservoir as if no flow barrier existed. The pEDFM model 16b exhibits pressure communication between both reservoir sides due to projection discontinuities, allowing undesired flow across the fracture. In contrast,

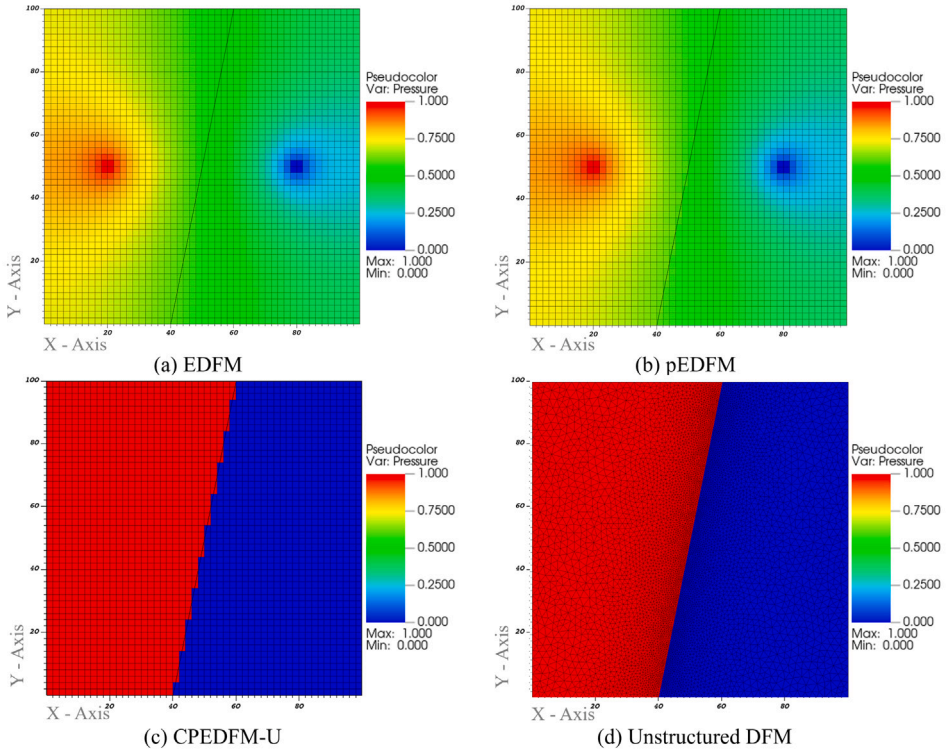

Fig. 16. Two-phase Flow in a Square Reservoir with Two Wells and an Inclined Barrier: Pressure fields for EDFM (a), pEDFM (b), CpEDFM-U (c), and Reference (d).

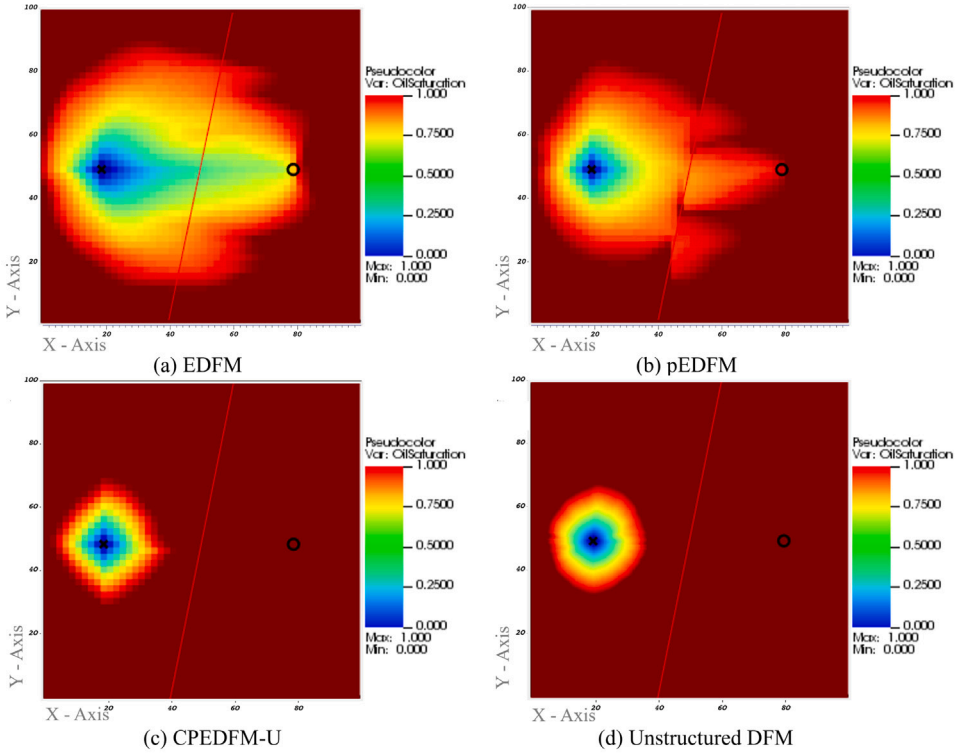

Fig. 17. Two-phase Flow in a Square Reservoir with Two Wells and an Inclined Barrier: Water saturation fields at PVI = 0.275 for EDFM (a), pEDFM (b), CpEDFM-U (c), and Reference (d).

both CpEDFM-U 16c and the reference solution 16d show a significant pressure contrast across the fracture, correctly representing its sealing behavior and preventing flow through it.

Fig. 17 presents the water saturation fields plotted at 25% of the total simulation time. At this stage, the EDFM model 17a completely disregards the fracture, allowing free fluid passage across it. The pEDFM

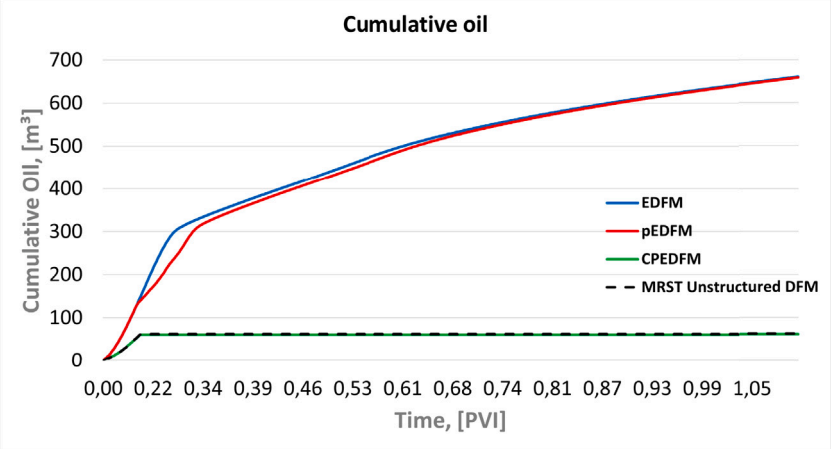

(a) Cumulative Oil

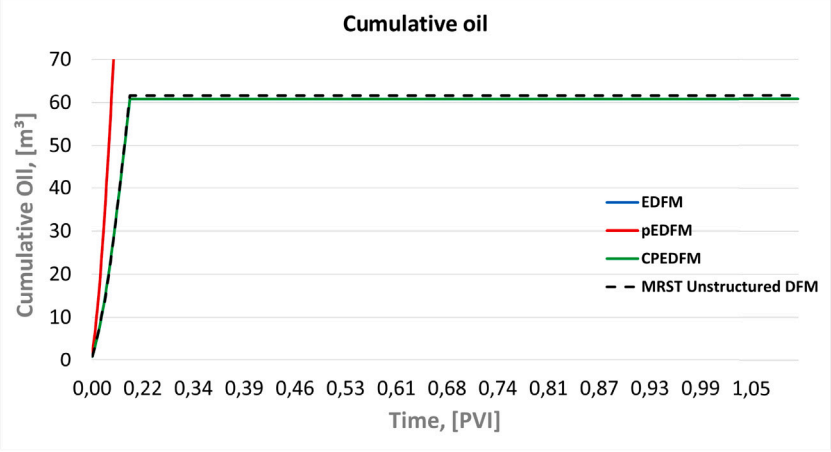

(b) Zoom highlighting CpEDFM-U and the unstructured DFM solutions.

Fig. 18. Two-phase Flow in a Square Reservoir with Two Wells and an Inclined Barrier: Cumulative oil production curves (EDFM, pEDFM, CpEDFM-U, and Reference).

results 17b reveal significant undesired leakage through the fracture due to projection discontinuities. This behavior is absent in both the CpEDFM-U 17c and the DFM grid reference solution 17d, which accurately represents the fracture as a flow barrier, effectively preventing water migration across it.

Fig. 18 shows the cumulative oil production curves over time. Both EDFM (blue line) and pEDFM (red line) models overestimate cumulative production, particularly in early simulation time. Our CpEDFM-U model (green line) closely matches the reference solution (black dashed line). The zoomed view in Fig. 18b better illustrates the agreement between CpEDFM-U and the MRST reference solution. It is possible to observe that, even in the CpEDFM-U and DFM models, where there is no communication between the wells, a small amount of oil is produced in the early stages of the simulation. This occurs due to the pressure difference between the producing well and the reservoir, which results in oil production through primary recovery. However, as the pressures stabilize, production ceases, which explains why the production lines of these methods become constant until the end of the simulation.

In Fig. 19 we present the water cut values that clearly show the CpEDFM-U efficacy in blocking fluid flow, mirroring the reference solution null water cut, different from EDFM and pEDFM.

The results demonstrate that conventional EDFM and pEDFM models fail to properly represent the hydraulic barrier effect of inclined sealing fractures in porous media. To evaluate method accuracy, we calculated the relative L2-norm of the error for cumulative oil production. CpEDFM-U showed the smallest error (3.41%), indicating excellent agreement with the reference, while pEDFM and EDFM exhibited significantly larger errors, 87.80% and 95.18%, respectively. This study further confirms CpEDFM-U as a significantly more accurate and reliable alternative for fractured reservoir simulations, particularly in waterflooding scenarios where production forecasting is critical for planning and decision-making. Its ability to correctly represent arbitrarily oriented sealing fractures makes it especially suitable for realistic applications in complex geological formations.

5. Conclusion

In the present paper, we present a new methodology for simulating two-phase oil and water flow in naturally fractured reservoirs. Using an enhanced approach based on Embedded Discrete Fracture Models (EDFM and pEDFM), we developed the CpEDFM-U model, which integrates continuous fracture projection, allowing the simulation of complex geometries with structured and unstructured two-dimensional (2D) meshes. Our model addresses the limitations of previous methods, such as the inability to accurately represent fractures with low conductivity and inclined fractures, by ensuring continuous projection, without discontinuities that compromise the accuracy of the results. Through a series of numerical simulations comparing CpEDFM-U with traditional EDFM and pEDFM methods, we demonstrate that CpEDFM-U excels in terms of accuracy. In scenarios involving inclined fractures, such as the example of a diagonal sealing barrier, CpEDFM-U outperforms traditional models, which exhibit significant errors due to

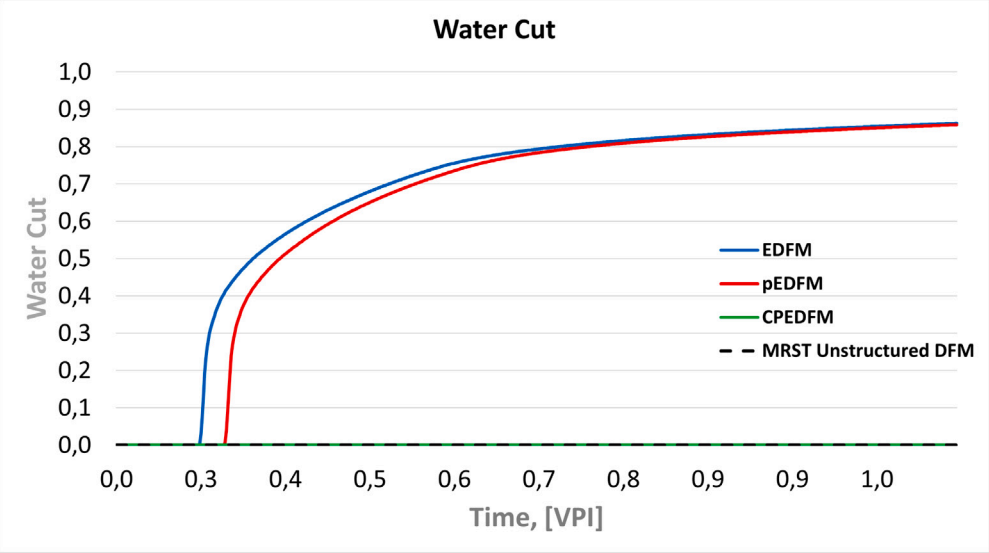

Fig. 19. Two-phase Flow in a Square Reservoir with Two Wells and an Inclined Barrier: Water Cut Curves for different methods of modeling fractures.

the lack of continuity in projections. The accuracy of CpEDFM-U was verified through comparison with reference solutions, showing very good agreement, even with coarse meshes. Additionally, the proposed model demonstrated great robustness in two-phase flow simulations, even in reservoirs with multiple fractures and varying geometric and permeability characteristics. CpEDFM-U not only accurately represents flow barriers and flow channels but also adapts efficiently to different fracture configurations. In terms of cumulative oil production, CpEDFM-U showed excellent correlation with the reference solution, while EDFM and pEDFM models overestimated production due to modeling errors in sealing fractures. Therefore, CpEDFM-U proves to be a powerful and efficient tool for realistic simulations in complex geological environments, with great potential for optimization in enhanced oil recovery scenarios and other related industrial processes.

CRediT authorship contribution statement

Gabriel Martins Cavalcanti Feitosa: Writing – review & editing, Writing – original draft, Software. **Emanoel Rodrigues dos Santos:** Writing – review & editing, Writing – original draft, Software. **Pedro Victor Paixão Albuquerque:** Writing – review & editing, Writing – original draft, Software, Methodology. **Artur Castiel Reis de Souza:** Software, Methodology, Conceptualization. **Darlan Karlo Elisiário de Carvalho:** Writing – review & editing, Supervision, Methodology, Conceptualization. **Paulo Roberto Maciel Lyra:** Writing – review & editing, Supervision, Methodology, Conceptualization.

Declaration of competing interest

The authors declare the following financial interests/personal relationships which may be considered as potential competing interests: Gabriel Martins Cavalcanti Feitosa reports financial support was provided by Energi Simulation. Gabriel Martins Cavalcanti Feitosa reports financial support was provided by Foundation for Support of Science and Technology of Pernambuco State. Emanoel Rodrigues dos Santos reports financial support was provided by National Council for Scientific and Technological Development. Pedro Victor Paixao Albuquerque reports financial support was provided by Foundation for Support of Science and Technology of Pernambuco State. Darlan Karlo Elisiario de Carvalho reports financial support was provided by National Council for Scientific and Technological Development. Paulo Roberto Maciel Lyra reports financial support was provided by National Council for Scientific and Technological Development. If there are other authors, they declare that they have no known competing financial interests or personal relationships that could have appeared to influence the work reported in this paper.

Acknowledgments

The authors would like to acknowledge the financial support provided by Science Support Foundation of the State of Pernambuco (FACEPE), Brazil, the National Council for Scientific and Technological Development (CNPq), Brazil and the Coordination for the Improvement of Higher Education Personnel (CAPES Foundation), Brazil. Funding: CNPq, Brazil (PQ-308334/2019-1 and PQ-310145/2021-0), and Energi Simulation grants 14/2025.

Data availability

Data will be made available on request.

References

Berkowitz, B., 2002. Characterizing flow and transport in fractured geological media: A review. Adv. Water Resour. 25 (8–12), 861–884.

Berre, I., Boon, W.M., Flemisch, B., Fumagalli, A., Gläser, D., Keilegavlen, E., Scotti, A., Stefansson, I., Tatomir, A., Brenner, K., et al., 2021. Verification benchmarks for single-phase flow in three-dimensional fractured porous media. Adv. Water Resour. 147, 103759.

Burbulla, S., Rohde, C., 2020. A fully conforming finite volume approach to two-phase flow in fractured porous media. In: International Conference on Finite Volumes for Complex Applications. Springer, pp. 547–555.

Cavalcante, T.d.M., Contreras, F.R.L., Lyra, P.R., de Carvalho, D.K.E., 2020. A multipoint flux approximation with diamond stencil finite volume scheme for the two-dimensional simulation of fluid flows in naturally fractured reservoirs using a hybrid-grid method. Internat. J. Numer. Methods Fluids 92 (10), 1322–1351.

Cavalcante, T.d.M., Souza, A.C., Hajibeygi, H., Carvalho, D.K., Lyra, P.R., 2024. Simulation of two-phase flow in 3D fractured reservoirs using a projection-based Embedded Discrete Fracture Model on Unstructured tetrahedral grids (pEDFM-U). Adv. Water Resour. 187, 104679.

Chen, Z., et al., 2007. Reservoir simulation.

Contreras, F.L., Lyra, P., Souza, M., Carvalho, D., 2016. A cell-centered multipoint flux approximation method with a diamond stencil coupled with a higher order finite volume method for the simulation of oil–water displacements in heterogeneous and anisotropic petroleum reservoirs. Comput. & Fluids 127, 1–16.

Dachanuwattana, S., Jin, J., Zuloaga-Molero, P., Li, X., Xu, Y., Sepehrnoori, K., Yu, W., Miao, J., 2018. Application of proxy-based MCMC and EDFM to history match a Vaca Muerta shale oil well. Fuel 220, 490–502.

de Hoop, S., Voskov, D., Bertotti, G., Barnhoorn, A., 2022. An advanced discrete fracture methodology for fast, robust, and accurate simulation of energy production from complex fracture networks. Water Resour. Res. 58 (5), e2021WR030743.

Dijkstra, E.W., 2022. A note on two problems in connexion with graphs. In: Edsger Wybe Dijkstra: His Life, Work, and Legacy. pp. 287–290.

Fumagalli, A., Keilegavlen, E., Scialò, S., 2019. Conforming, non-conforming and non-matching discretization couplings in discrete fracture network simulations. J. Comput. Phys. 376, 694–712.

Gao, Z., Wu, J., 2011. A linearity-preserving cell-centered scheme for the heterogeneous and anisotropic diffusion equations on general meshes. Internat. J. Numer. Methods Fluids 67 (12), 2157–2183.

Hajibeygi, H., Karvounis, D., Jenny, P., 2011. A hierarchical fracture model for the iterative multiscale finite volume method. J. Comput. Phys. 230 (24), 8729–8743.

HosseiniMehr, M., Tomala, J.P., Vuik, C., Al Kobaisi, M., Hajibeygi, H., 2022. Projection-based embedded discrete fracture model (pEDFM) for flow and heat transfer in real-field geological formations with hexahedral corner-point grids. Adv. Water Resour. 159, 104091.

Jiang, J., Younis, R.M., 2017. An improved projection-based embedded discrete fracture model (pEDFM) for multiphase flow in fractured reservoirs. Adv. Water Resour. 109, 267–289.

Karim-Fard, M., Firoozabadi, A., 2003. Numerical simulations of water injection in fractured media using the discrete-fracture model and the Galerkin method. SPE 83633: Soc. Pet. Eng. 117–126.

Karimi-Fard, M., Durlofsky, L.J., Aziz, K., 2004. An efficient discrete-fracture model applicable for general-purpose reservoir simulators. SPE J. 9 (02), 227–236.

Kim, S., 2017. Numerical Methods for Partial Differential Equations. Department of Mathematics and Statistics, Mississippi University, USA.

Lake, L.W., Johns, R., Rossen, B., Pope, G.A., et al., 2014. Fundamentals of enhanced oil recovery, vol. 1, Society of Petroleum Engineers Richardson, TX.

Li, L., Lee, S.H., 2008. Efficient field-scale simulation of black oil in a naturally fractured reservoir through discrete fracture networks and homogenized media. SPE Reserv. Eval. Eng. 11 (04), 750–758.

Mejia, C., Roehl, D., Rueda, J., Quevedo, R., 2021. A new approach for modeling three-dimensional fractured reservoirs with embedded complex fracture networks. Comput. Geotech. 130, 103928.

Moinfar, A., Varavei, A., Sepehrnoori, K., Johns, R.T., 2014. Development of an efficient embedded discrete fracture model for 3D compositional reservoir simulation in fractured reservoirs. SPE J. 19 (02), 289–303.

Olorode, O., Wang, B., Rashid, H.U., 2020. Three-dimensional projection-based embedded discrete-fracture model for compositional simulation of fractured reservoirs. SPE J. 25 (04), 2143–2161.

Rao, X., 2023. A generic workflow of projection-based embedded discrete fracture model for flow simulation in porous media. Comput. Geosci. 27 (4), 561–590.

Rao, X., Cheng, L., Cao, R., Jia, P., Liu, H., Du, X., 2020. A modified projection-based embedded discrete fracture model (pEDFM) for practical and accurate numerical simulation of fractured reservoir. J. Pet. Sci. Eng. 187, 106852.

Rao, X., Guo, S., He, X., Kwak, H., Hoteit, H., 2025. A first streamline-based simulation method within the projection-based embedded discrete fracture model (pEDFM). Comput. Geotech. 185, 107357.

Rao, X., Guo, S., He, X., Kwak, H., Yousef, A., Hoteit, H., 2024a. Hybrid mimetic finite difference and streamline methods for numerical simulation of two-phase flow in fractured reservoirs. Comput. Geotech. 166, 106048.

Rao, X., He, X., Du, K., Kwak, H., Yousef, A., Hoteit, H., 2024b. A novel projection-based embedded discrete fracture model (pEDFM) for anisotropic two-phase flow simulation using hybrid of two-point flux approximation and mimetic finite difference (TPFA-MFD) methods. J. Comput. Phys. 499, 112736.

Rao, X., Liu, Y., 2022. A numerical modelling method of fractured reservoirs with embedded meshes and topological fracture projection configurations. Comput. Model. Eng. Sci. 131 (3), 1403–1429.

Rashid, H.U., Olorode, O., 2024. A continuous projection-based EDFM model for flow in fractured reservoirs. SPE J. 29 (01), 476–492.

Ren, G., Jiang, J., Younis, R.M., 2018. A model for coupled geomechanics and multiphase flow in fractured porous media using embedded meshes. Adv. Water Resour. 122, 113–130.

Rostami, S., Boukadi, F., Bodaghi, M., et al., 2023. Review of embedded discrete fracture models: Concepts, simulation and pros & cons. Pet. Petrochem. Eng. J. 7 (2), 1–15.

Sandve, T.H., Berre, I., Nordbotten, J.M., 2012. An efficient multi-point flux approximation method for discrete fracture–matrix simulations. J. Comput. Phys. 231 (9), 3784–3800.

Shakiba, M., 2014. Modeling and Simulation of Fluid Flow in Naturally and Hydraulically Fractured Reservoirs Using Embedded Discrete Fracture Model (EDFM) (Ph.D. thesis).

Teixeira, J., Carvalho, D., Cavalcante, T., Angelim, K., Lyra, P., 2022. Numerical simulation of oil-water displacements in naturally fractured reservoirs using a hybrid grid MPFA-streamline (SLS-HyG) formulation. Comput. Geotech. 151, 104963.

Ţene, M., Bosma, S.B., Al Kobaisi, M.S., Hajibeygi, H., 2017. Projection-based embedded discrete fracture model (pEDFM). Adv. Water Resour. 105, 205–216.

Wang, Q., Moridis, G.J., Blasingame, T.A., 2023. Wavelet transforms for the simulation of flow processes in porous geologic media. Transp. Porous Media 146 (3), 771–803.

Wang, L., Wang, Y., Vuik, C., Hajibeygi, H., 2022. Accurate modeling and simulation of seepage in 3D heterogeneous fractured porous media with complex structures. Comput. Geotech. 150, 104923.

Xu, J.C., Zhou, W.X., Li, H.Y., 2023. Efficient production optimization for naturally fractured reservoir using EDFM. Pet. Sci. 20 (4), 2268–2281.

Yu, W., Xu, Y., Liu, M., Wu, K., Sepehrnoori, K., 2018. Simulation of shale gas transport and production with complex fractures using embedded discrete fracture model. AIChE J. 64 (6), 2251–2264.

Zeng, Q.D., Yao, J., Shao, J., 2019. Study of hydraulic fracturing in an anisotropic poroelastic medium via a hybrid EDFM-XFEM approach. Comput. Geotech. 105, 51–68.